

Wintertime process study of the North Brazil Current rings reveals the region as a larger sink for CO₂ than expected

Léa Olivier¹, Jacqueline Boutin¹, Gilles Reverdin¹, Nathalie Lefèvre¹, Peter Landschützer², Sabrina Speich³, Johannes Karstensen⁴, Matthieu Labaste¹, Christophe Noisel¹, Markus Ritschel², Tobias Steinhoff⁴ and Rik Wanninkhof⁵

¹ LOCEAN-IPSL, Sorbonne Université-CNRS-IRD-MNHN, Paris, France

² Max Planck Institute for Meteorology, Hamburg, Germany

³ Laboratoire de Météorologie Dynamique, ENS-Ecole Polytechnique-CNRS-Sorbonne Université, Paris, France

⁴ GEOMAR Helmholtz Centre for Ocean Research, Kiel, Germany

10 ⁵ Atlantic Oceanographic & Meteorological Laboratory of NOAA, Miami, USA

Correspondence to: Léa Olivier (lea.olivier@locean.ipsl.fr)

Abstract.

15 The key processes driving the air-sea CO₂ fluxes in the western tropical Atlantic (WTA) in winter are poorly known. WTA is a highly dynamic oceanic region, expected to have a dominant role on the variability of CO₂ air-sea fluxes. In early 2020 (February), this region was the site of a large in-situ survey and studied in wider context through satellite measurements. The North Brazil Current (NBC) flows northward along the coast of south America, retroflects close to 8°N and pinches off the world's largest eddies, the NBC rings. The rings are formed to the north of the Amazon River mouth when freshwater discharge
20 is still significant in winter (a time period of relatively low runoff). We show that in February 2020, the region [50°W-59°W – 5°N-16°N] is a CO₂ sink from the atmosphere to the ocean (-1.7 TgC.month⁻¹), a factor of 10 greater than previously estimated. The spatial distribution of CO₂ fugacity is strongly influenced by eddies south of 12°N. During the campaign, a nutrient rich freshwater plume from the Amazon River is entrained by a ring from the shelf up to 12°N leading to high phytoplankton concentration and significant carbon drawdown (~20 % of the total sink). In trapping equatorial waters, NBC
25 rings are a small source of CO₂. The less variable North Atlantic subtropical water extends from 12°N northward and represents ~60 % of the total sink due to their lower temperature associated with winter cooling and strong winds. Our results, in identifying the key processes influencing the air-sea CO₂ flux in the WTA, highlight the role of eddy interactions with the Amazon River plume. It sheds light on how lack of data impeded a correct assessment of the flux in the past, and on the necessity of taking into account features at meso and small scale.

1 Introduction

The North Brazil Current (NBC) is one of the dominant features of the tropical Atlantic circulation. In a region dominated by zonal jets, it flows northward along the coast of South America and separates from the coast around 6-8°N. The NBC seasonally turns back on itself in a tight loop, called the NBC retroflexion, and feeds the North Equatorial Counter Current, closing off the equatorial wind-driven gyre (Figure 1). This retroflexion occasionally pinches off some of the world's largest eddies, the North Brazil Current rings (Johns et al., 1990; Richardson et al., 1994).

After their separation from the NBC retroflexion region, the rings travel north-westward toward the Lesser Antilles in a course parallel to the coast of South America. These eddies have been extensively studied using modelling and both, in-situ (e.g. 1998-2001 NBC Ring experiment, Wilson et al., 2002) and satellite observations (e.g. Goni & Johns, 2001, Fratantoni & Glickson, 2002, Aroucha et al., 2020). They have a mean radius of 200 km and their diameter can exceed 450 km. Vertically, some of them extend down to more than 1000 m (Fratantoni and Glickson, 2002; Fratantoni and Richardson, 2006; Johns et al., 2003). The NBC rings swirl clockwise and travel with an average north-westward translation speed of 8-15 km d⁻¹ (Johns et al., 1990; Mélice and Arnault, 2017). Most of the anticyclonic eddies detectable by altimetry are rather shallow, extending from the surface to 200-300 m (Garraffo et al., 2003; Wilson et al., 2002). When they reach the Lesser Antilles, they start to coalesce and disintegrate, partly due to interactions with the topography (Fratantoni and Richardson, 2006; Jochumsen et al., 2010). There is substantial variability in the number of rings shed per year, ranging from 5 (Aroucha et al., 2020; Fratantoni and Glickson, 2002; Mélice and Arnault, 2017; Goni and Johns, 2001) to 9 (Johns et al., 2003). NBC rings play a crucial role in the interhemispheric transport of salt and heat in the Atlantic Ocean and are an important part of the meridional overturning circulation (Johns et al., 2003). The NBC rings disrupt an already complex region located in the vicinity of the Amazon River mouth and at the transition between equatorial and subtropical waters. While most of the studies on rings focused on their physical properties, little is known about their biogeochemical properties and how they affect the air-sea CO₂ flux of the western tropical Atlantic.

The global ocean acts as an atmospheric CO₂ sink, taking up 23% of total anthropogenic CO₂ emissions (Friedlingstein et al., 2020) and leading to ocean acidification (IPCC, 2021; 2019). The concentration of atmospheric CO₂ is increasing due to human activities (IPCC, 2019; 2021), and characterizing the role of the ocean in mitigating climate change through CO₂ uptake is thus a key investigation. The equatorial Atlantic Ocean is the second-largest source of CO₂ to the atmosphere after the equatorial Pacific (Landschützer et al., 2014; Takahashi et al., 2009). Previous works in this region examined the influence of the equatorial upwelling and of the Amazon plume on the CO₂ flux. CO₂-rich equatorial waters, originating from the equatorial upwelling (Andrié et al., 1986) strongly contrast with the CO₂-undersaturated Amazon River plume waters. The magnitude of the Amazon River discharge is unique in the global ocean. It represents as much freshwater as the next 7 largest rivers in the world combined and contributes to almost 20% of global river freshwater input to the ocean (Dai and Trenberth, 2002). It

65 therefore strongly impacts the physical, biogeochemical and biological properties of the coastal and the open ocean. Often
overlooked, the Amazon River plume is an atmospheric CO₂ sink of global importance (Ibáñez et al., 2016). The plume
carries water rich in silicate, nitrogen and phosphate into the tropical oceanic waters that are strongly depleted in nutrients. As
water mixes and turbidity decreases, the primary producer's growth and associated biological drawdown are stimulated (Chen
et al., 2012). Nitrogen is rapidly consumed, and nitrogen fixation by diazotrophs becomes the main pathway of carbon
70 sequestration in the plume (Subramaniam et al., 2008). This strong carbon drawdown leads to a significant sink of atmospheric
CO₂ (Körtzinger, 2003; Lefèvre et al., 2010). Not taking into account the Amazon plume would result in overestimating the
tropical Atlantic air-sea CO₂ flux by 10% (Ibáñez et al., 2016).

The Amazon River's discharge reaches a minimum in December and progressively increases from January onwards. The
75 plume extension is minimum from January to March (Fournier et al., 2015) and as a result, it is the period of maximum salinity
in the northwestern tropical Atlantic. The Amazon outflow region is particularly hard to reconstruct due to its strong variability
and a severe lack of data. Waters located in the southeasternmost part of the domain act as a strong source of CO₂ to the
atmosphere. The source gradually turns into a sink north of 10°N as waters become colder due to seasonal winter cooling. This
situation is typical of a transition zone between equatorial and subtropical waters in winter (Landschützer et al., 2020, Figure
80 1b). The northwestern tropical Atlantic is commonly divided into two parts, the northern much less variable part (also called
"Trade wind region"), and the southern part, also referred as Eddy Boulevard (Stevens et al., 2021). The freshwater of the
Amazon remains mainly confined to the continental shelf due to winds perpendicular to the coast as it travels northwestward
into the Caribbean Sea (Coles et al., 2013). However, it has recently been documented that off-shore freshwater transport is
often present in February and significantly alters the physical properties of the region (Reverdin et al., 2021). This is partly
85 due to the interaction of the NBC rings with the Amazon plume (Figure 1a). The ocean color signature of the Amazon (Muller-
Karger et al., 1988) has been used as a tracer to delineate the rings, and better understand their generation, evolution and
characteristics (Johns et al., 1990; Fratantoni & Glickson, 2002). The Amazon River also influences the surface temperature
and salinity of the rings. For example, Figure 1a shows a freshwater plume stirred by a large ring. They are considered warm-
core rings but have a warm SST anomaly in the first half of the year, and a cold one in the second half, because the anomaly
90 is relative to the regional SST, with an extensive warm pool in late summer and autumn (Ffield, 2005). Their signature in
salinity is therefore plume-dependent as well. Ffield (2005) reported that 3 out of 4 rings were surrounded by lower salinity
water. Salinity and chlorophyll-a are therefore critical to understand the surface physical and biogeochemical properties of the
region, as well as the air-sea fluxes of CO₂.

95 The northwestern tropical Atlantic is a dynamically active region, with eddies several hundred kilometers in diameter and
connected to the world's largest river. There are surprisingly few biogeochemical observations available for winter months
during low outflow of the Amazon River. Few tropical Atlantic measurements of biogeochemical tracers are available with
one transect in winter in the Surface Ocean CO₂ Atlas (SOCAT, (Bakker et al., 2016) database south of 10°N crossing the

region. This scarcity is a major impediment in understanding the biological and physical processes underlying the oceanic carbon and nutrient cycles in the region. Satellite salinity shows a contrasted spatial structure, with eddies and filaments (Figure 1a). In this study, we take advantage of the physical and biogeochemical data collected during the EUREC⁴A-OA/ATOMIC experiment in January-February 2020, combined with satellite data, to understand how the NBC rings and their related structures impact the air-sea CO₂ flux in winter. The paper is organized as follows. We present the in-situ observational data from the EUREC⁴A-OA/ATOMIC experiment as well as the satellite data in section 2. We identify the water masses observed in the region, their physical and biogeochemical properties and estimate the CO₂ fluxes at regional scale using empirical relationships in section 3. In section 4, we compare the results with climatologies of air-sea CO₂ fluxes to evaluate the added knowledge brought by the intensive surveys of February 2020. We discuss the results and the interannual variability in section 4 and we conclude in section 5.

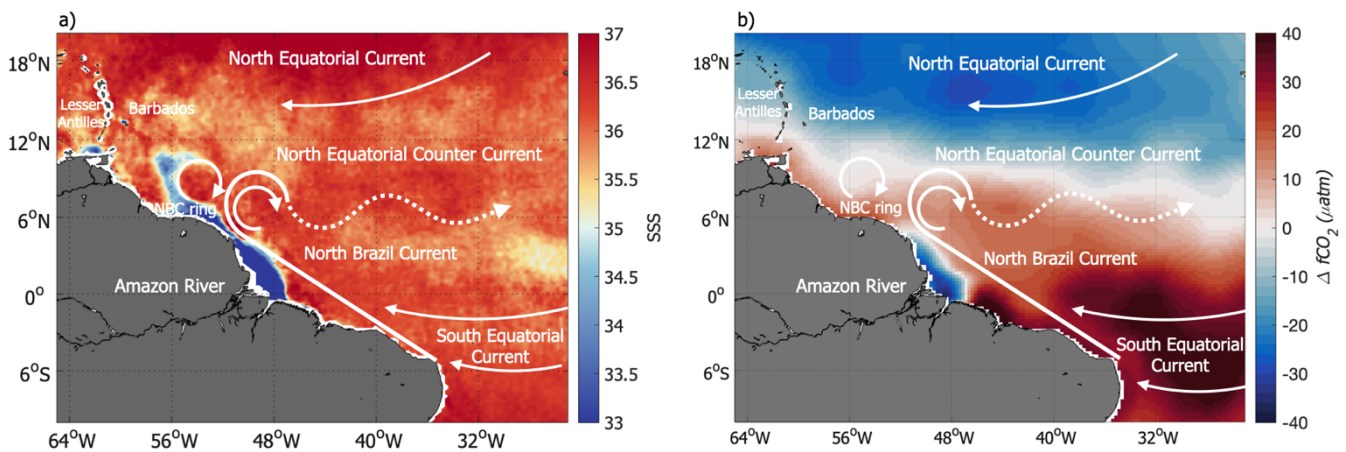


Figure 1: Schematic of the main ocean currents in the western tropical Atlantic superimposed over the SSS field of Feb. 7th 2017 (a) and over the February $\Delta f\text{CO}_2$ climatology from Landschützer et al., 2020 (b).

115 2 Data and Methods

2.1 In-situ data

The EUREC⁴A-OA (Elucidating the Role of Clouds-Circulation Coupling in Climate Ocean-Atmosphere) / ATOMIC (Atlantic Tradewind Ocean Mesoscale Interaction Campaign, Stevens et al., 2021) campaign took place in January and February 2020 and involved research vessels (RV) from France (RV Atalante, Speich and The Embarked Science Team, 2021), Germany (RV Maria S. Merian, hereby designated as Merian, Karstensen et al., 2020 and RV Meteor, not considered in this

study since no CO₂ measurements were taken onboard), and the United States (RV Ronald H. Brown, hereby designated as Ron Brown, Quinn et al. 2021). These cruises provided numerous in-situ measurements and, in this study, we will focus on the continuous near surface measurements of temperature, salinity and fCO₂.

125 Temperature and salinity from thermosalinographs (TSG), as well as fCO₂, were measured from water pumped ~5 m below
the surface. For each ship, the resulting CO₂ data is corrected (Lefèvre et al., 2010; Pierrot et al., 2009) from the temperature
difference between the water at the ship's water intake and the one analyzed by the instrument. The RV Atalante fCO₂
measurements started on January 30th and ended on February 18th 2020 (Olivier et al., 2020). The underway oceanic and
atmospheric fCO₂ were detected by infrared detection using a Licor 7000 (Takahashi et al., 1993). The fCO₂ system was the
130 same as in Lefèvre et al. (2010). It uses a shower air-sea equilibrator described by Poisson et al. (1993). Seawater from the
TSG pumping circuit circulates in the equilibrator at a rate of 2 L.min⁻¹. A closed-loop of about 100 mL of air flows through
the equilibrator designed to avoid bubbles at the air-sea interface. To minimize temperature corrections, the equilibrator is
thermostated with the same seawater as the one used for CO₂ measurements. The temperature difference between the
equilibrator and the sea was on the order of 0.5 °C.

135 Furthermore, 138 samples for dissolved inorganic carbon (DIC) and total alkalinity (TA) analysis were collected onboard RV
Atalante as well as inorganic nutrients (silicate, phosphate, nitrate and nitrite). DIC and TA were measured at the SNAPO-
CO₂ facility by potentiometric titration using a closed cell, following the method of Edmond (1970). Nutrients were conserved
by heat pasteurization and analysed by colourimetry at IRD LAMA service in Brest.

An OceanPackCUBE ferrybox system from SubCtech was installed on the RV Merian measuring continuously the oceanic
140 fCO₂ from the 23rd of January to the 19th of February 2020. Water is pumped at a rate of ~7 L.min⁻¹ through a debubbler unit
subsequently followed by a SeaBird SBE 45 thermosalinograph before it circulates along a membrane through which CO₂
diffuses. On the other side of the membrane, the air-loop is circulated at a rate of 0.5 L.min⁻¹ through a Li-COR LI840 non-
dispersive infrared gas analyzer (e.g., Arruda et al., 2020). The RV Ron Brown completed two legs, from January 10th to
January 25th and from January 29th to February 13th 2020. The General Oceanic Inc. 8500 pCO₂ instrument installed onboard
145 follows a similar methodology to the underway fCO₂ system deployed on the Atalante and is detailed in Pierrot et al. (2009).

An intercomparison of the fCO₂ measured by the RVs Atalante and Merian is attempted when the ships were navigating
together at a distance less than 5 km (Figure 2). On average, the fCO₂ measured by the RV Merian is 6.4 µatm higher than the
one measured on the RV Atalante, with a standard deviation of 4.8 µatm. The RVs Merian and Ron Brown crossed the same
150 water mass at 13-14°N/57°W on February 12th. On average, the RV Merian fCO₂ is 6 µatm higher than the RV Ron Brown
fCO₂. In part we link these differences to the slower response time of the membrane system, however differences also lie
within the uncertainties of the fCO₂ observing systems (~5µatm for the membrane system installed on the RV Merian (see
Arruda et al., 2020) and ~2 µatm for the equilibrator systems installed on the RVs Atalante and Ron Brown). The region where

RV Merian and RV Atalante were close is very variable (standard deviation of $20 \mu\text{atm}$), and the RV Merian and RV Ron Brown were never in the same place at the same time, so that the observed differences could also be due to the natural variability of fCO_2 sampled differently by the various ships. Hence, we did not apply any correction and we checked that the effect of a $6 \mu\text{atm}$ systematic bias on the RV Merian fCO_2 has a minor effect on our resulting interpolations. A comparison between the reconstructed flux with and without a correction for the $6 \mu\text{atm}$ systematic bias suggests that such a systematic bias would lead to less than $2 \mu\text{atm}$ difference on our mean interpolated fCO_2 and less than $0.1 \text{ mmol.m}^{-2}.\text{day}^{-1}$ on the mean derived air-sea CO_2 flux.

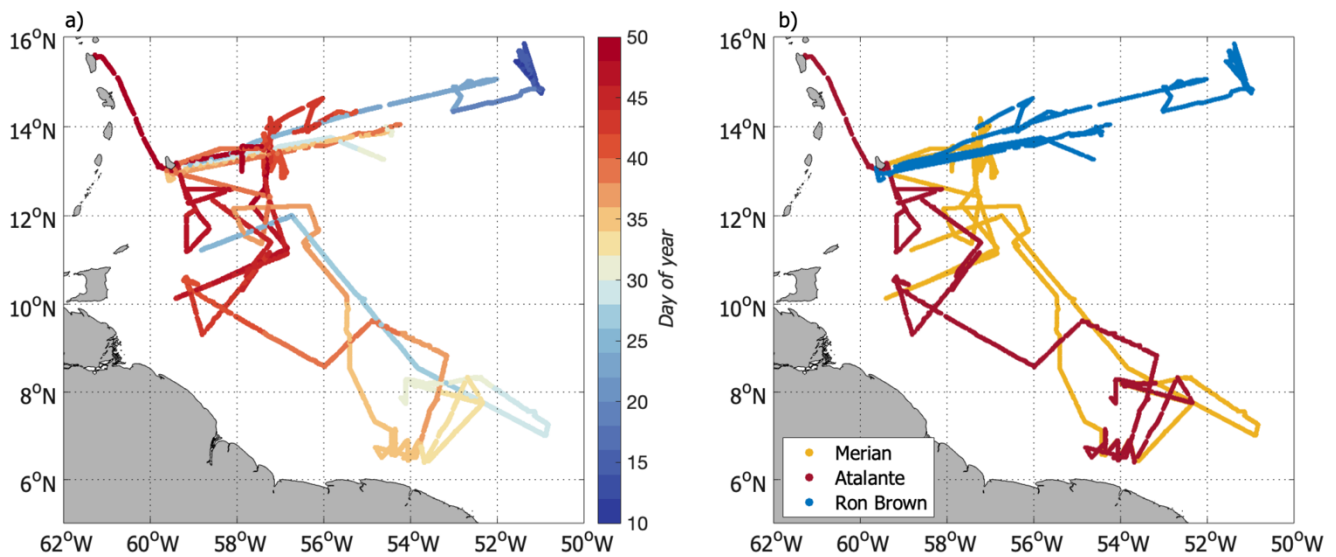


Figure 2: Ship tracks colour-coded by day of year (a) and by ship name (b).

165 2.2 Satellite and atmospheric reanalyzes data

Daily satellite maps of chlorophyll-a (Chla), sea surface temperature (SST), as well as absolute dynamic topography (ADT) and sea surface salinity (SSS) are used in this study.

The salinity maps are a blend of the Soil Moisture Ocean Salinity (SMOS, Jan. 2010-present), and Soil Moisture Active Passive (SMAP, Apr. 2015-present) measurements developed by Reverdin et al. (2021). The European SMOS and US SMAP missions observe the sea surface by L-band radiometry from sun-synchronous polar-orbiting satellites (Entekhabi et al., 2010; Font et al., 2009; Kerr et al., 2010; Piepmeier et al., 2017). Combining 6 a.m. and 6 p.m. measurements of both missions provides an

almost complete coverage each day. When the coverage was not complete over our region, the 6 a.m. track of the following day was also included. This daily field is available for the first 20 days of February, and leaves out only 2 days without sufficient coverage to retrieve salinity data. It has a spatial resolution close to 70 km, and an uncertainty on the order of 0.5. This product is optimized for the northwestern tropical Atlantic in February 2020 and has an almost daily resolution. It is an experimental daily product built to have the best representation possible of the Amazon plume variability. The product, its uncertainties and the comparison between the TSG salinity and the satellite SSS are detailed in Reverdin et al. (2021).

Daily Chl a concentration maps and SST maps are produced by CLS (Stum et al., 2016) on a spatial grid of 0.02° . The Chl a concentration maps are composites built from VIIRS (on Suomi-NPP and NOAA-20 US platforms) and OLCI (on Sentinel 3A and 3B Copernicus European platforms) satellite sensors. The SST product is a 1-day average of 4 infrared radiometer satellite data. Both datasets are sensitive to the cloud cover, but during our period of interest, they are usually without many gaps except at the end of February. Comparison between the TSG SST and the satellite SST product are detailed in the RV Atalante cruise report (Speich & The Embarked Science Team, 2021).

Daily ADT maps at a $\frac{1}{4}^\circ$ resolution combine data from all satellites available for the period 1993 to present. From these ADT fields, the TOEddies algorithm, developed by Laxenaire et al. (2018), identifies eddies and their trajectories. The eddy detection is based on the closed contours of ADT, as well as the maximum geostrophic velocity associated to the eddy.

In order to compute the air-sea CO $_2$ fluxes, the European Centre for Medium-Range Weather Forecasts (ECMWF) Reanalysis v5 (ERA5) hourly wind speed and mean sea level pressure, P_{atm} , is used. ERA5 covers the period from January 1950 to present, and provides hourly data on a 30 km grid. In addition, the monthly wind speed and SST fields over the period 1998-2015 are used, and a climatology over this period is computed. The wind speed in the region in winter is on average between 6 and 8 m s^{-1} and its variability is low.

We compare the EUREC 4 A-OA/ATOMIC observations with the observation-based CO $_2$ partial pressure ($p\text{CO}_2$) climatology developed by Landschützer et al., (2020), created using a 2-step neural network method (Landschützer et al., 2016) and combining open and coastal ocean datasets. The associated $\Delta p\text{CO}_2$ and air-sea CO $_2$ flux monthly field climatologies over the 1998-2015 period are computed using the ERA5 climatological wind, SST and P_{atm} fields as well as the atmospheric CO $_2$ from the Ragged Point, Barbados station.

2.3 Methods

2.3.1 Air-sea CO $_2$ flux

We compute the air-sea flux (F ; $\text{mmol.m}^{-2}.\text{day}^{-1}$) as:

$$205 \quad F = k \cdot K_0 \cdot (fCO_2 - fCO_{2atm}) \quad (1)$$

Where K_0 is the solubility of CO_2 in seawater, expressed as a function of SSS and SST by Weiss (1974); fCO_{2atm} is the atmospheric CO_2 fugacity; and k is the gas transfer velocity. k is calculated following the relation from Wanninkhof (2014):

$$k = 0.251 \cdot \langle U^2 \rangle \cdot (Sc/660)^{-0.5} \quad (2)$$

where Sc is the Schmidt number and U is the wind speed at 10 m above sea level derived from ERA5 wind speed. The ERA5
210 wind speed is used for the satellite-based analysis and the air-sea CO_2 flux climatology. The measured winds from the ships are adjusted to 10 m following a logarithmic profile (Tennekes, 1973) and used to compute the along-track flux for visualisation purposes.

In order to compute fCO_{2atm} over that period, we first derived the saturation vapor pressure (P_{H_2O}) from SSS and SST then the atmospheric pCO_2 using the monthly averaged CO_2 mole fraction (xCO_{2atm}) measured at the NOAA/Earth System Research
215 Laboratory (ESRL) station in Ragged Point, Barbados (13.17°N, 59.43°W):

$$fCO_{2atm} = xCO_{2atm} \cdot (P_{atm} - P_{H_2O}) \cdot C_f \quad (3)$$

Where C_f is the fugacity coefficient, function of the atmospheric pressure and SST (Weiss, 1974).

2.3.2 Reconstruction of fCO_2 from satellite maps

220 Our approach is to derive from the large EUREC⁴A-OA dataset a relationship linking fCO_2 to SST, SSS and $Chla$ in order to provide maps of fCO_2 based on the satellite maps of SST, SSS and $Chla$. $Chla$ was not measured onboard, thus, we use satellite surface $Chla$ co-located along the ship track. This set of parameters is used as proxy to describe the influence of ocean dynamics, chemistry, and also marine biology on fCO_2 . The biological carbon pump is one of the major components of the oceanic and global carbon cycles, as the photosynthetic production of organic carbon by marine phytoplankton accounts for
225 about half of the carbon fixation associated with global primary production (Arrigo, 2007; Behrenfeld et al., 2006; Field et al., 1998). However, while $Chla$ is an indicator of biological activity, it is also a very good tracer of ocean circulation so that, depending on the water masses origin, fCO_2 and $Chla$ are not expected to be systematically negatively correlated. Waters rich in detrital material tends to limit the phytoplankton growth and microbial respiration of riverine material on the continental shelf likely dominates (Aller and Blair, 2006; Medeiros et al., 2015; Mu et al., 2021). Even considering the extend of the
230 EUREC⁴A-OA atomic cruise, the dataset is still sparse, and cannot fully represent the small-scale variability it highlights. In order to understand the fluxes at regional scale the need for a good spatial resolution arises. For that, the surface T-S- $Chla$ diagram computed from the ship measurement (and collocated satellite $Chla$) is interpolated using a linear 3D interpolation on a grid of SST, SSS and $Chla$. The grid has a resolution of 0.01°C in SST, 0.1 in SSS, and 0.01 in $\log(Chla \text{ (mg m}^{-3}\text{)})$. Using a 3D linear interpolation to mapping the fCO_2 data over a grid is a simple yet effective solution for a dataset that is still relatively
235 sparse. The method is presented in more details in the supplementary materials (Text S1). Using a linear fit prevents oscillations between two data points, and yields good results. Along the ship track, the standard deviation between the measured and

reconstructed $f\text{CO}_2$ is $\sim 4 \mu\text{atm}$. To each triplet of surface T, S, and $\log(\text{Chla})$ in the range of the values measured by the ship is therefore associated a value of $f\text{CO}_2$ based on the 3D linear interpolation of the in-situ values. In order to cover the whole range of T-S- $\log(\text{Chla})$ present in the region, we extrapolate to lower temperatures and lower salinities than the ones measured by the ship. In order to do so, we add 4 points to the T-S- Chla diagram at lower salinities and lower temperatures based on previous knowledge of the region. For the low salinity domain ($\text{SSS} < 30$), $f\text{CO}_2$ is strongly dominated by salinity and the influence of temperature is weak (Lefèvre et al., 2010). The SSS- $f\text{CO}_2$ relation developed by Lefèvre et al. (2010) is in good agreement with the SSS- $f\text{CO}_2$ relationship computed from this study data (supplementary Figure S1) in the common range, we therefore use it to compute $f\text{CO}_2$ at a salinity of 26 ($f\text{CO}_2(\text{S} = 26) = 251.4 \mu\text{atm}$). The lower temperature is mostly located in the northern part of the domain, that is the least variable and where the variations of $f\text{CO}_2$ are dominated by the ones in temperature. From this dataset we compute a variation of $15 \mu\text{atm}/^\circ\text{C}$, which is consistent with the $4.23\% \text{ }^\circ\text{C}^{-1}$ expected variation of $f\text{CO}_2$ with temperature due to the temperature sensitivity of the carbonate dissociation constants and CO_2 solubility (Takahashi et al., 2002; Wanninkhof et al., 1999). We use this dependency to compute the $f\text{CO}_2$ at a temperature of 24°C to cover the whole range of temperature in the region.

250

We combine the interpolated $f\text{CO}_2$ with satellite maps of SST, SSS and Chla to obtain daily high-resolution maps of $f\text{CO}_2$. Some days, either the presence of clouds altering the Chla and SST and the lack of salinity coverage prevent the retrieval of $f\text{CO}_2$. In order to limit the error on $f\text{CO}_2$, we only keep 9 days out of the 20 first days of February (2, 4, 6, 7, 9, 11, 12, 17 and 19 of February) where the coverage is sufficient. Then, daily mean sea level pressure maps and wind fields are used to compute the air-sea CO_2 flux over the region in a similar way as described in 2.3.1. The salinity maps present major errors near islands, because no correction of the island effect was applied on the SMAP maps (Grotsky et al., 2018). Therefore, the reconstructed flux will be studied over a region excluding the close vicinity of the islands [59°W - 50°W , 5°N - 16°N].

255

3 Results

3.1 A transition region presenting a strong mesoscale activity

260

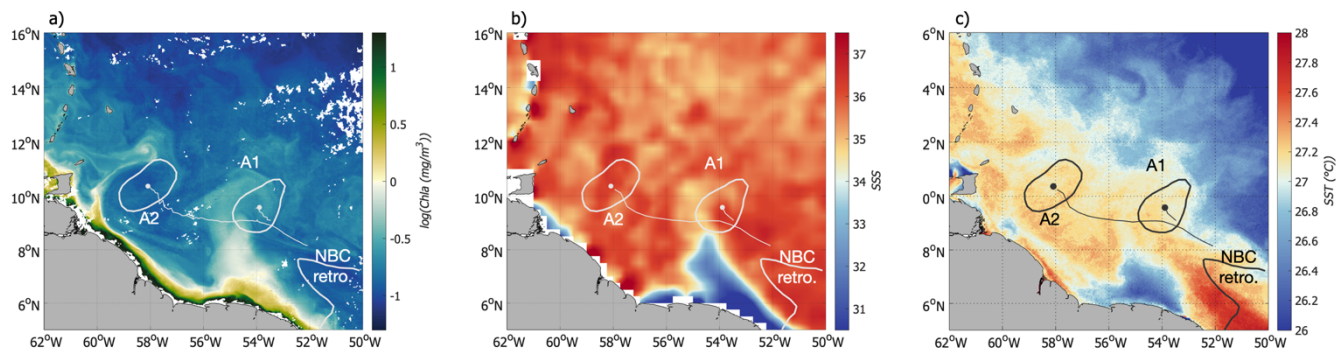


Figure 3: a) Chlorophyll-a, b) SSS and c) SST on Feb 6th 2020 with the contours of NBC rings A1 and A2, their centre and their trajectory. The NBC retroflection is identified from the 0.51 m contour of the satellite derived ADT.

Figure 3 shows how in February 2020, the ocean currents of the WTA strongly influence the variability of SSS, SST and Chla
 265 at many scales, with an NBC ring stirring a plume of fresher water rich in chlorophyll-a toward the open ocean. This is also supported by the measurements done during the EUREC⁴A/ATOMIC campaign in January-February 2020 (Figure 4). They show a complex environment, for example ΔfCO_2 presents similar large-scale features as the climatology, but it also reveals numerous smaller scale structures (Figure 4a). Among the latter, two stand out. These are the very low fCO_2 in the south-eastern part of the domain, and the high fCO_2 around 11°N. In early 2020, the NBC retroflection was very variable and shed
 270 two large anticyclonic rings (Figure 3). They are long-lived 250-km large eddies traveling north-westward toward the Lesser Antilles in the Eddy Boulevard region. The ring detection algorithm TOEddies based on ADT indicates that NBC ring A2 separated from the retroflection in late December, was fairly stationary during the cruise period (February 2020) and located around 58°W-11°N. NBC ring A1 separated from the retroflection in early February 2020 and then stayed around 54°W-10°N for 10 days before translating northwestward toward the Lesser Antilles after the 20th of February. These eddies contribute to
 275 the variability of the region in two ways. As they travel, they transport the water trapped in their core during their formation (eddy trapping), but they also stir the surrounding waters (eddy stirring).

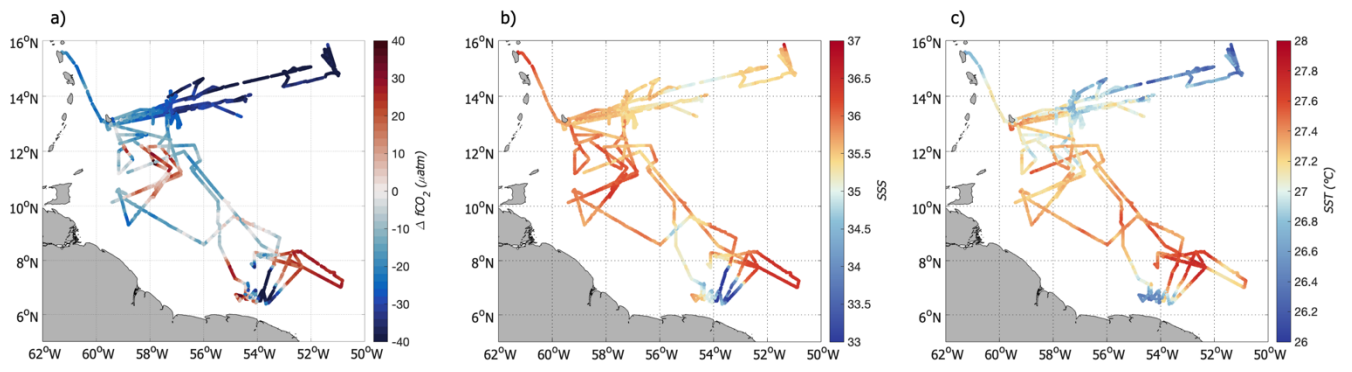
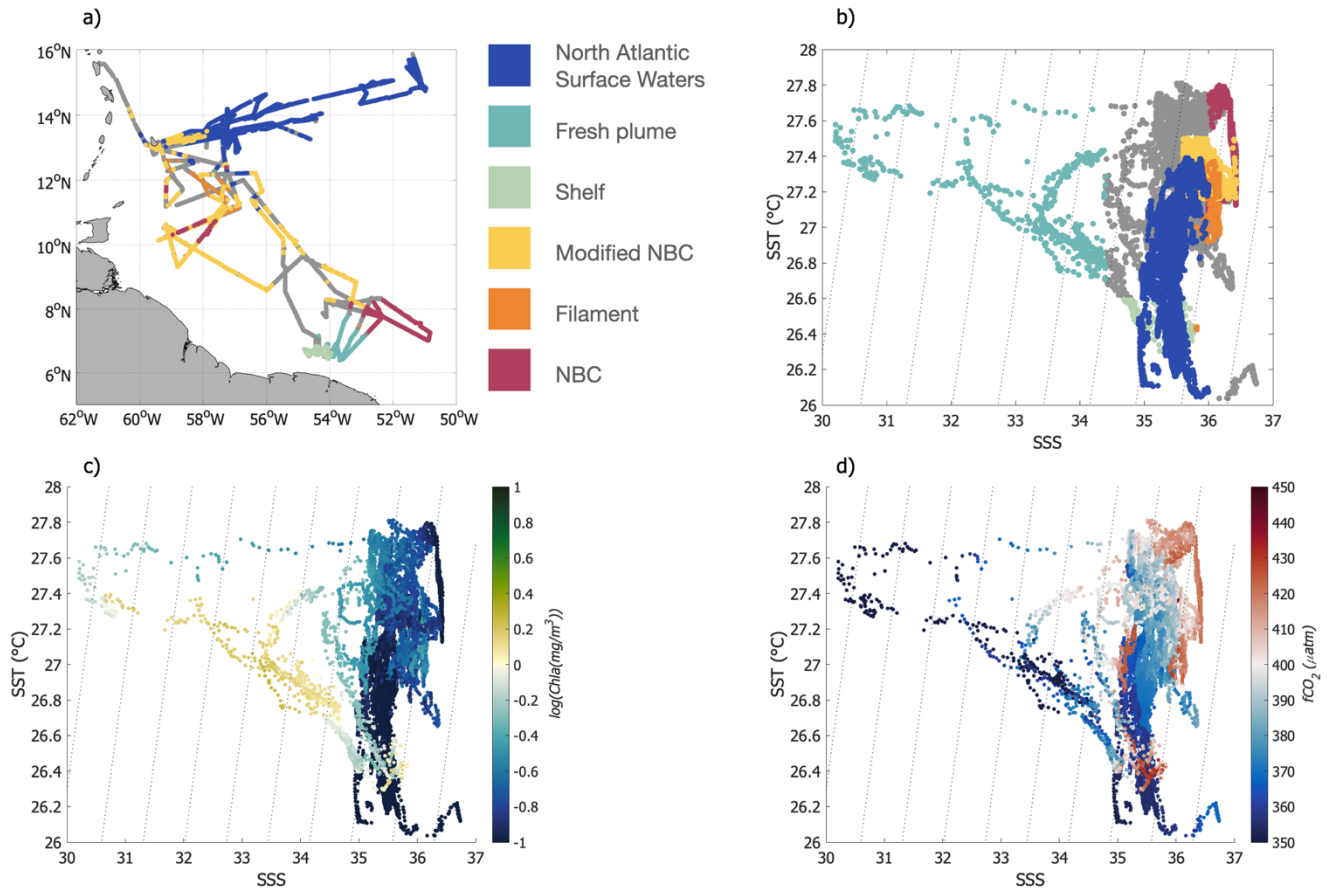


Figure 4: In-situ measurements of (a) $\Delta f\text{CO}_2$, (b) salinity, (c) temperature.

280 3.2 Surface water masses identification



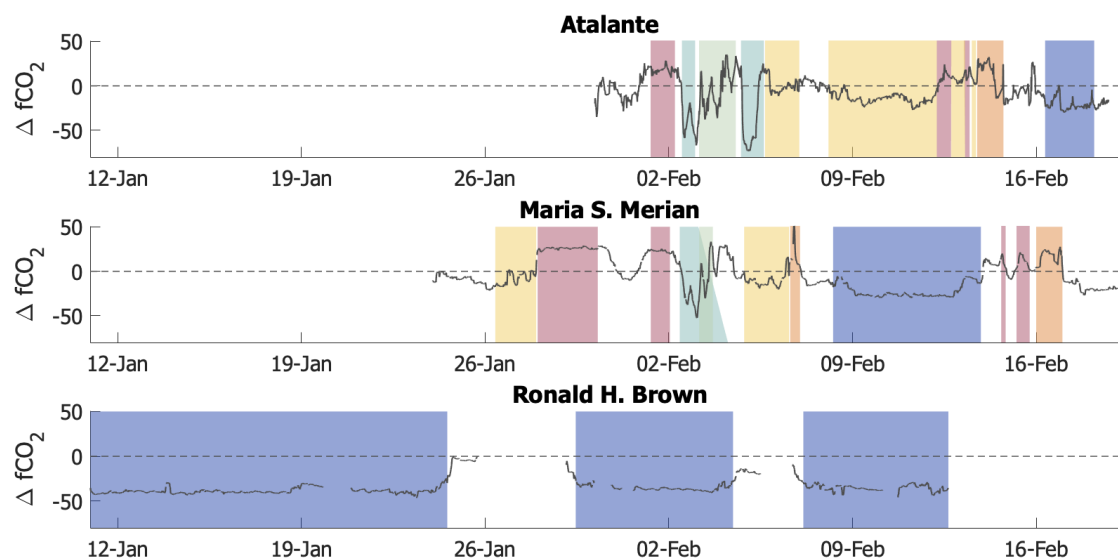
285 **Figure 5: a) Map representing the RVs Atalante, Merian and Ron Brown ship tracks colour-coded with the identified water masses. b) T-S diagram colour-coded with the water masses; the grey colour corresponds to points that do not fit into the definition of the identified water masses.**

In an effort to understand how biogeochemistry is forced by physical processes in the ocean, we used surface *Chla* to complement SST and SSS data in defining surface water masses. We observed that in the northwestern tropical Atlantic in winter in situ $f\text{CO}_2$ strongly depends on these three variables (Figure 4, Figure 5). There is a strong positive dependence of $f\text{CO}_2$ on SSS, with low $f\text{CO}_2$ for low SSS (Figure 5c-d). Across the whole EUREC⁴A-OA/ATOMIC region, SST did not vary much (mean SST of 27°C, and standard deviation of 0.5°C), but warmer waters present higher $f\text{CO}_2$. The dependence on *Chla* allows for the discrimination of water masses with the same surface TS properties but not the same $f\text{CO}_2$ (Figure 5). Satellite-based *Chla* is hard to discriminate from detrital material using ocean colour where both are present as they have close spectral characteristics. Figure 5 shows that waters with an SST of 26.5°C and SSS between 35-36 can either be rich in *Chla* and have a high $f\text{CO}_2$ or low in *Chla* and have a low $f\text{CO}_2$. By combining SST and SSS with *Chla* and using information from the dynamical structures of the region, we identified six upper-ocean water masses (Figure 5a-b). The along track $\Delta f\text{CO}_2$ for each ship is presented on Figure 6, colour-coded with the identified water mass, highlighting the link between the surface T-S-*Chla* relation and $\Delta f\text{CO}_2$. The way we defined water masses, considering time-varying boundaries, is relatively similar to the one used by Longhurst (2010), and some of the surface water masses compare well with Longhurst (2010) biogeochemical provinces. He identified 3 provinces in the Northwestern tropical Atlantic, The North Atlantic Tropical Gyre province (NATR), the Western Tropical Atlantic province (WTRA) and the Guianas Coastal province. In this first part, we will present two surface water masses that are usually identified in the region (e.g. Longhurst et al., 1995, 2010) and their physical properties. North of Barbados, the domain is mostly dominated by North Atlantic Subtropical Waters (NASW), similar to Longhurst's NATR. They have a SSS in the range of 35 to 36 and are relatively cold (Table 1). Their SST diminishes over time towards the end of February. These waters are less influenced by coastal dynamics and therefore are not very productive at the surface (*Chla* levels inferior to 0.14 mg.m⁻³) due to low nutrient levels. They are mainly located north of 13°N, and get progressively colder toward the north-east. The RV Ron Brown stayed in that Trade Wind region for almost a month (Figure 5). The observations collected from this ship show NASW lower $f\text{CO}_2$ with respect to the atmosphere ($\Delta f\text{CO}_2 \sim -40\mu\text{atm}$). Similar results are found on one of the RV Merian's transect, with $\Delta f\text{CO}_2 < -30\mu\text{atm}$.

310 The NBC is surface-intensified and fed by the central branch of the South Equatorial Current (SEC, Schott et al., 1998). As the cold and saline water from the upwelling region is transported westward by the SEC, it warms up (SST > 27°C), but retains its saline characteristic (SSS > 36, Table 1) as it reaches the NBC retroflexion region (Figure 4). This NBC water mass is oligotrophic (Figure 3b), and therefore in our area of interest distinguished itself by its low level of surface *Chla* (*Chla* < 0.14 mg.m⁻³). These waters are found in the retroflexion area, and sampled by both RVs Merian and Atalante at the beginning of February (Figure 5). The NBC water mass is in some way similar to the WTRA, but does not extend beyond the retroflexion,

315

therefore representing a more limited part of the WTRA. We will introduce four new water masses in the following parts, as well as their associated dynamical structures. They can be considered as subsets of the WTRA and Guiana Coastal province, these two provinces being too large and not well suited to represent small-scale processes.



320

Figure 6: RVs Atalante (top), Merian (middle) and Ron Brown (bottom) ΔfCO_2 time-series. The background color indicates the crossed water mass domains (see definition in legend of Fig 5).

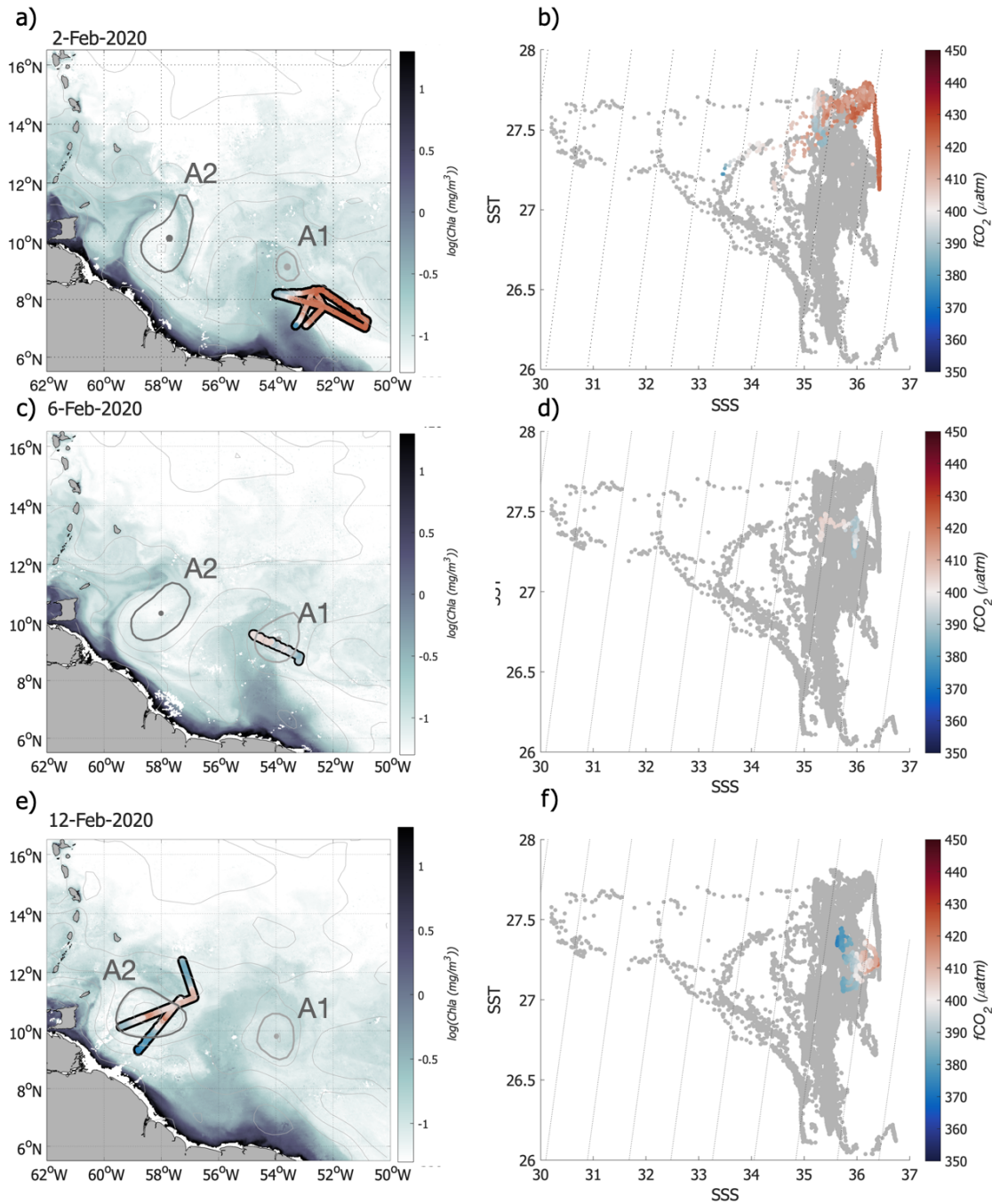
	NASW	NBC	Modified NBC	Freshplume	Shelf	Filament
Temperature (°C)	<27.2	> 27	27.16 < SST < 27.6		< 26.6	< 27.4
Salinity	35 < SSS < 36	> 36	> 35.6	< 34.5		35.8 < SSS < 36.3
Chlorophyll-a (mg.m ⁻³)	< 0.14	< 0.14	0.11 < Chla < 0.25	> 0.25	> 0.25	> 0.25

Table 1. Thresholds in SSS, SST and Chla used to define the 6 water masses identified in the winter WTA.

3.3 North Brazil Current rings

The extension of the NBC retroflection varies depending on the state of eddy formation. It moves northwestward up until 9°N as an eddy is forming, and then retracts to the southeastern part of the region. During our period of interest, the retroflection shed anticyclone A1 at the beginning of February. It is difficult to estimate the date of shedding as the area is highly dynamic and detecting the first closed contour of ADT is complicated and may be inaccurate. It is however interesting that the two ships sampled the retroflection when it was expanding to generate A1, and this northwestward expansion is well observed on several physical and biogeochemical parameters (Figure 7a). RV Merian crossed the retroflection on January, 27th and stayed in the area until February, 2nd (Figure 6). Chl*a* present on the shelf is advected by the strong currents on the periphery of the retroflection and delineates well its south-western side (Figure 7a). The NBC waters stand out on the surface TS diagram, as they are the most saline waters observed in the region (Figure 7b). They are also high in fCO₂ which reflects their equatorial origin. Their SST is relatively warm, varying from 27.8 °C at the crossing of the first retroflection front, to 27.2 °C. The region is rather homogeneous, with an almost constant SSS of 36.3 and ΔfCO₂ along the multiple crossings, as observed on the Merian and Atalante transects (Figure 6). On average along those transects, the NBC fCO₂ is higher than fCO_{2atm} by 20 μatm.

Anticyclone A1 is further crossed by the RV Atalante on February 6th, just a few days after its separation from the retroflection (Figure 7c). The surface signal is almost lost, both in SST and in fCO₂ (Figure 7c-d). It is mainly composed of modified NBC water, which properties are close to the NBC water (high SSS, high SST, low Chl*a*) but not as pronounced. This water mass covers a larger area, which mainly encompasses the Eddy Boulevard region. It is defined here as $SSS > 35.6$, $27.16\text{ °C} < SST < 27.6\text{ °C}$ and $0.11\text{ mg m}^{-3} < Chl\textit{a} < 0.25\text{ mg m}^{-3}$ (Table 1). While the high Chl*a* water delimits well the retroflection area, it partly covers the eddy A1.



345 **Figure 7:** a) RVs Atalante and Merian ship track in the NBC retroflection (Merian: Jan. 27th to Feb. 2nd, Atalante: Feb 2nd), c) in NBC ring A1 (Atalante: Feb 6th) and e) in NBC ring A2 (Atalante: Feb 12th-13th, Merian: Feb 13th-14th) colour-coded with fCO₂. The background represents the Chla on Feb 2nd (a), Feb 6th (c) and Feb 12th (e), and the contours of NBC rings A1 and A2 are indicated. b),d),f) Corresponding T-S diagrams colour-coded with fCO₂.

350 NBC ring A2 presents a different situation. Detached from the retroflection in early December 2019 (as defined from altimetry detection), it travelled north-westward while retaining an intense coherent core. Coastal waters identified by their high *Chla* content were less present and mostly entrained at the north-westward edge of the eddy. After two months, A2 almost reached Trinidad and Tobago and was located around 11°N/58°W when it was sampled by the two ships (Figure 7e). The SST signal is eroded, and most of the eddy is mostly made of modified NBC water with relatively low $f\text{CO}_2$. However high SSS (36.5) and $f\text{CO}_2$ (415 μatm) are still visible near the eddy centre on the two crossings made by RV Atalante on the 12th and 13th of February. This is confirmed by the two sections of the Merian that crossed the altimetric eddy centre and measured SSS 0.5 higher in the 50 km radius around the centre and above 36. The NBC water mass is therefore found close to the centre of eddy A2, as well as its associated high $f\text{CO}_2$.

360 From the collected observations, it appears that the surface signature of NBC rings is relatively variable and complex. It is well marked in their formation area in the NBC retroflection, where waters brought north by the NBC are warmer, saltier, and higher in $f\text{CO}_2$ than the water of the northwestern tropical Atlantic. As the eddies travel northwestward, further away from the retroflection, they may be subject to various processes that modify the surface signal. Unfortunately, the data collected is not sufficient to shed light on which processes are involved in this situation. South of Barbados, away from the retroflection, the modified NBC is therefore the most common water mass. Nevertheless, the NBC water is still sometimes observed months after the separation from the retroflection, in the eddy centre.

3.4 Freshwater plume

The NBC rings form and evolve in an area highly influenced by the Amazon River plume. Even if February is a period of low Amazon River outflow (Dai & Trenberth, 2002), freshwater events are relatively common. In February 2020, a freshwater plume detached from the Guiana plateau and spread out into the northwestern tropical Atlantic. The off-shelf plume was steered northward by the retroflection and NBC ring A1 up to 12°N and then extended westward toward the Caribbean Sea. Waters carried by the plume strongly contrast with the saline waters of the retroflection. They include water from the Amazon and present low SSS (SSS < 34.5), low $f\text{CO}_2$ ($f\text{CO}_2$ < 380 μatm) and high *Chla* (Table 1). The plume was crossed three times, twice on February 2nd and once on February 5th (Figure 6). Freshwater from the Amazon arrived on the plateau on the 1-2nd of February and was then entrained northwestward by Ekman transport and geostrophic currents (Reverdin et al., 2021). On the 2nd of February RVs Atalante and Merian left the retroflection area to cross the adjacent nascent plume. SSS rapidly decreased, reaching 33 which is associated to a strong decrease of $f\text{CO}_2$ (Figure 8). From the 2nd to the 5th of February, the plume formed and on February 5th the plume is approximately 100 km wide, with lowest salinities around 30. Based on satellite SSS data of the following days, the plume appears to have reached even lower salinities and then spread out over the north-western tropical

Atlantic. It first spread northward, steered by A1 and then northwestward, channelled between A1 and A2 reaching all the way up to 12°N and extending over more than 100 000 km² (Reverdin et al., 2021). The plume can be followed by satellite SSS and Chl*a* maps (Figures 7a, c, e). Indeed, the low SSS is also accompanied by high Chl*a* as water from the Amazon are considered highly productive. The north-western tropical Atlantic is in general nutrient-limited but the nutrients brought by the Amazon can support the occurrence of a bloom. The plume is also characterized by high silicate (between 4 and 10 μmol kg⁻¹ in the plume, almost 0 elsewhere), while nitrate and phosphate are rapidly consumed. Traces of inorganic phosphorus were observed in the plume, while nitrates were absent from surface waters (Supplementary Figure S2). Low salinity combined with high biological productivity led to low fCO₂ and a strong carbon drawdown in the plume, as the ΔfCO₂ reached -73 μatm on February 5th (Figure 6).

385 In an area highly influenced by the NBC waters, through rings or the retroflection, the plume stands out and modifies the biogeochemical dynamics of the region.

390

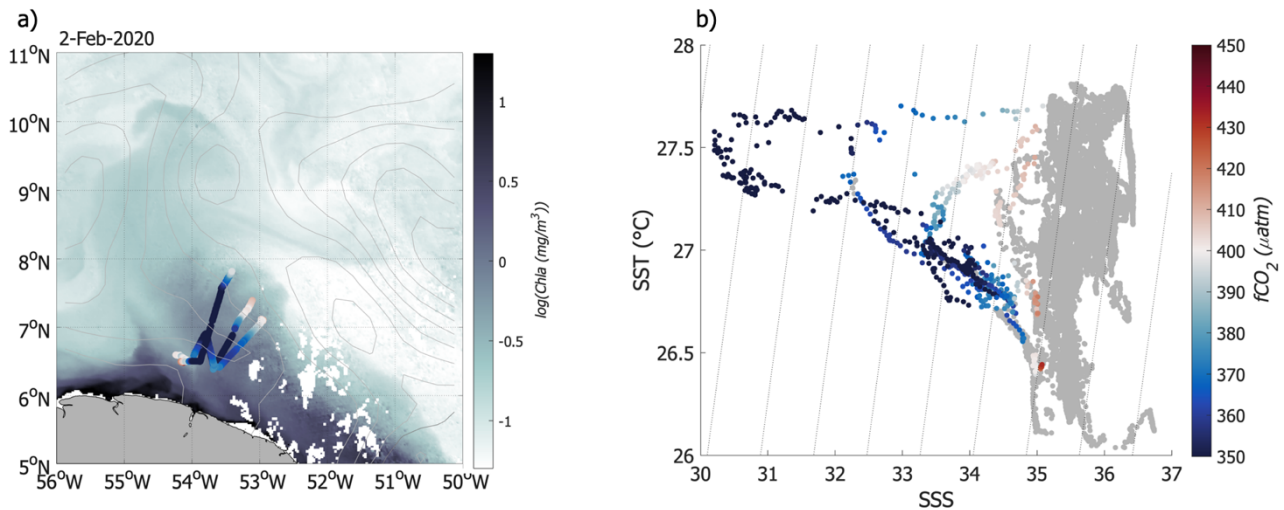


Figure 8: a) RVs Atalante and Merian ship track in the freshwater plume (Atalante: Feb 2nd, Feb 5th, Merian: Feb 2nd) colour-coded with fCO₂. The background represents the Chl*a* on Feb 2nd. b) Corresponding T-S diagram colour-coded with fCO₂.

395

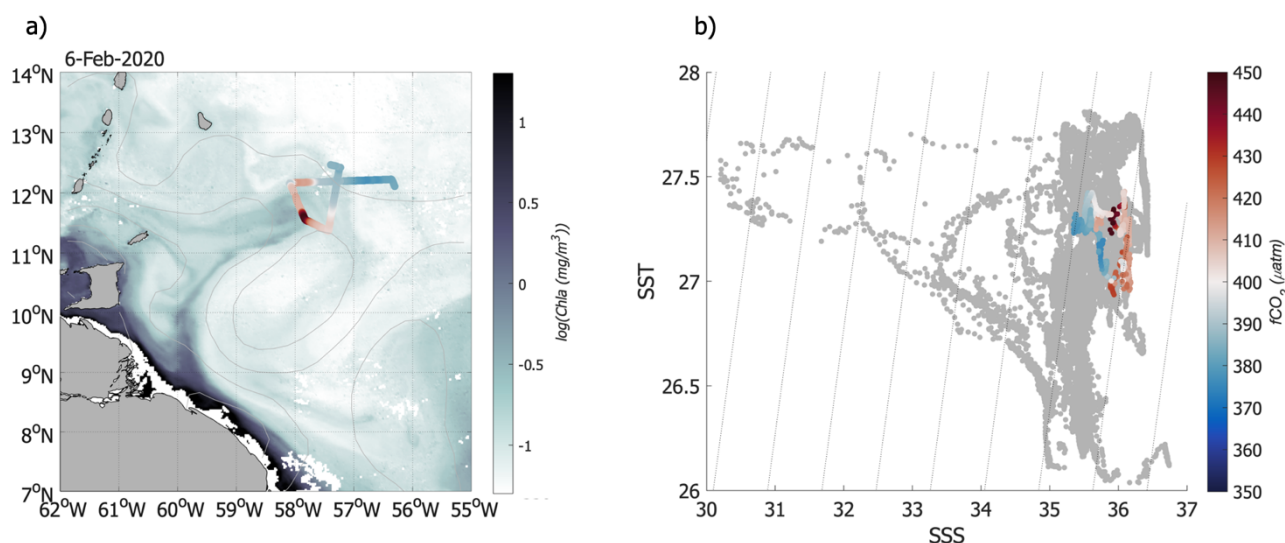
3.5 Shelf water and filaments

The freshwater plume is not the only water stirred by the NBC rings travelling from the NBC retroflection towards the Lesser Antilles. The shelf water is very different from the plume water, and was only sampled sparsely on the way in and out of the plume (Figures 4,5). On the Guiana plateau water is very rich in Chl*a* and detrital material, rather saline (SSS ~ 35.5) and relatively cold (SST ~ 26.5°C) (Figure 5, Table 1). Since the water sampled on the edge of the plume was cold due to a local

400

upwelling event (and/or vertical mixing event) detailed in the supplementary materials (Figure S3), temperature is not homogenous on the shelf.

Further north, a filament is stirred on the western side of NBC ring A2 (Figure 9a). It is a small-scale structure, approximately 10 km wide, easily identifiable due to its high Chla. The filament is continuously stirred by A2, and so is already visible on Chla maps of February 2nd (Figure 7). It followed A2's westward translation and was crossed on February 6th and 17th by RV Merian, and on February 14th by RV Atalante (Figure 6). It has a SSS close to 36, and an SST between 27°C and 27.5°C, thus it is slightly colder and more saline than its surrounding waters (Figure 9b, Table 1). It stands out by its high Chla content (Chla > 0.25 mg m⁻³), even if this is lower than close to the coast or in the freshwater plume. The strongest signal is observed on the ocean carbon parameters. In contrast to the freshwater plume, this filament presents very high fCO₂ (> 430 µatm), highlighting different origins. It stands out from the ship track time series by also having a larger positive ΔfCO₂ (50 µatm). Whereas the freshwater plume observed more southeastward carries water recently arrived on the plateau from the Amazon, the northwestward filament contains shelf waters.



415 **Figure 9:** a) RV Merian ship track in the shelf water filament (Feb 6th) colour-coded with fCO₂. The background represents the Chl_a on Feb 6th. b) Corresponding T-S diagram colour-coded with fCO₂.

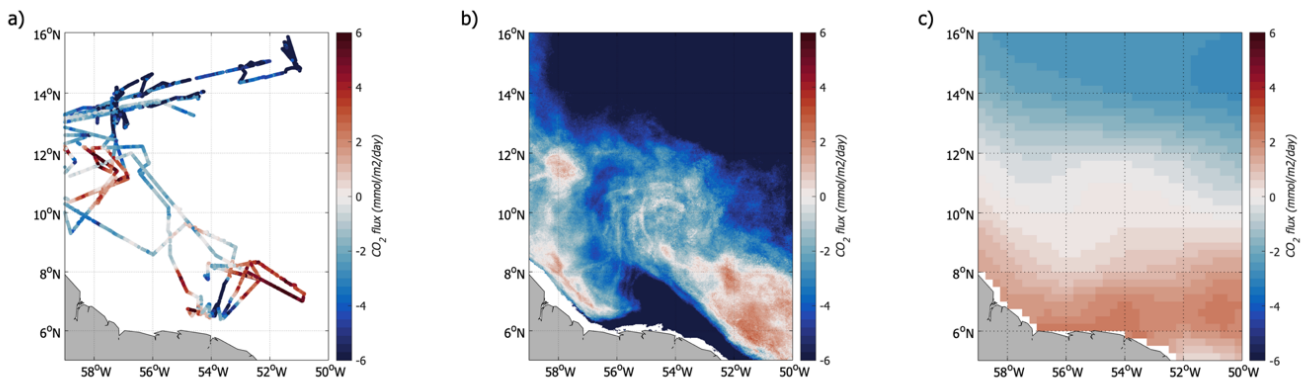
3.6 Air-sea CO₂ flux

In order to better characterize the impact of each structure on the regional flux, we computed air-sea CO₂ flux maps from satellite data, at a resolution of 2.5 km (Figure 10), averaged over the period of the cruise (February 2nd to February 19th). The along-track flux represented on Figure 10a and the reconstructed regional field (Figure 10b) show the importance of the small-scale dynamical structures, and highlights two strong regimes that are found on the reconstructed map. The air-sea CO₂ flux

in the northeastern part of the domain, characterized by the NASW, is mainly dominated by temperature effects while further south the presence of NBC rings, and their interactions with costal waters, create a strong dependence of the CO₂ flux on SSS and on the biological and biogeochemical processes highlighted by the Chla.

425

We evaluate the integrated air-sea CO₂ flux over the region. In February, waters are the coldest, and the region is a strong CO₂ sink of -1.7 TgC month⁻¹ (Figure 11). Three biogeochemical domains mainly contribute to the air-sea CO₂ flux, the NASW, the freshwater plume and the NBC retroflection. The impact on the flux of the small-scale coastal filament is evident along the ship tracks (Figure 10b). However, its contribution to the total flux is weak as the signal is smoothed when averaging over
 430 February 2nd to 19th, as the filament moves following the A2 ring northwestward translation. Each of the main three regions is identified based on its averaged SST, SSS and Chla properties in February and the region-specific flux is determined (Figure 11).



435 **Figure 10:** a) Air-sea CO₂ flux measured in Jan-Feb 2020 during the EUREC⁴A-OA/ATOMIC cruise. b) Air-sea CO₂ flux reconstructed over February 2020. c) February climatology of the air-sea CO₂ flux over 1998-2015 (Landschützer et al., 2020).

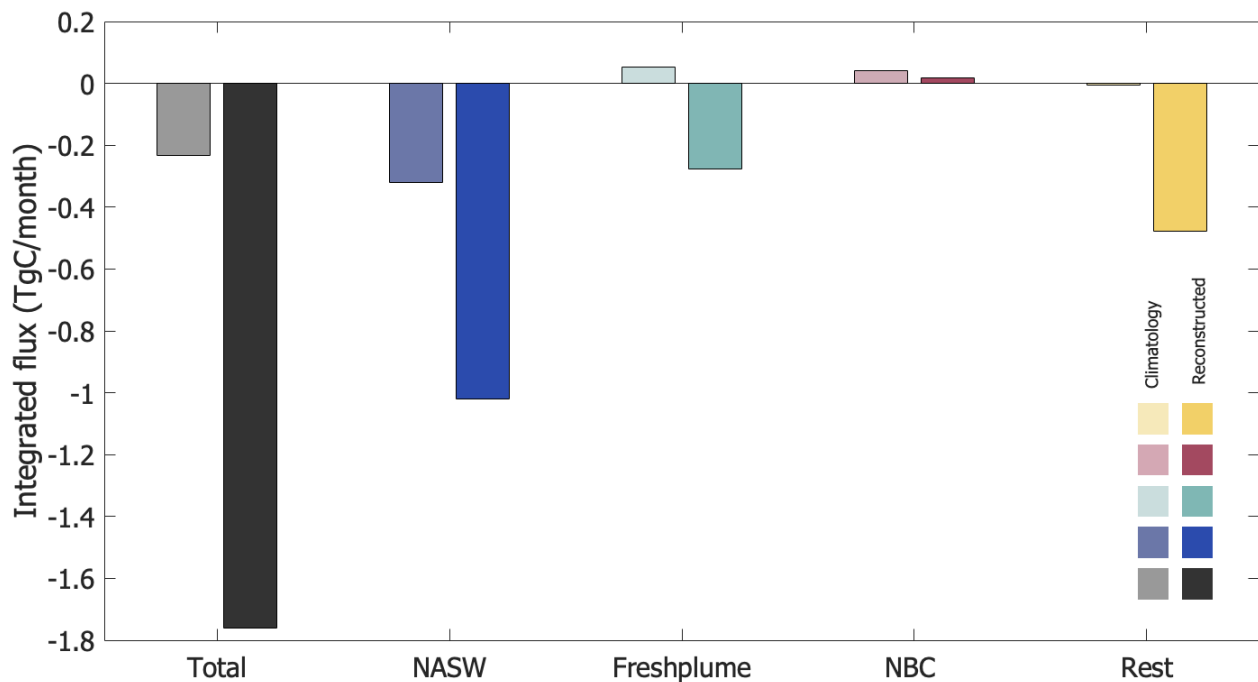
NASW contributes to about 60% of the total sink due to their relatively cold temperature and to strong winds that enhances the air-sea exchanges. These waters extend from Barbados northward and eastward, cover more than 1/3 of the domain and
 440 show a weak variability over February 2nd to 19th.

The NBC retroflection is a source of CO₂ to the atmosphere. In February, the strongest signal is observed in the southeastern part of the domain up to 8°N/53°W. The retroflection nevertheless impacts the region as far as 10°N/54°W as it is spatially variable, reaching up to 10°N when shedding an eddy. The two NBC rings present a small positive February air-sea CO₂ flux
 445 average. Eddy A1 is almost stationary from its formation date (around February 6th) until February 20th and its neutral to

slightly positive CO₂ flux is centred around 10°N/54.5°W (Figure 10). Eddy A2 translates rapidly westward at the beginning of February, and then northward from the 15th of February. Its signal is therefore not as visible as on the ship tracks as it is averaged over 19 days. The retroflexion is the main region with a positive air-sea CO₂ flux, even if the region is too small to have a big global impact, understanding small-scale features may be significant for the total flux. The NBC rings carry part of the signal, which is heavily modified as they travel northwestward. As a result, on average in early to late February only the retroflexion maintains a positive flux, while a large part of the domain dominated by modified NBC waters (non-influenced by the plume) behaves as a small sink.

The freshwater plume with Amazon water is nascent when crossed by the ships (Figure 10b), but is already the strongest signal of the time-series. As the plume develops, it is entrained by NBC ring A1, then A2 and spreads out into the open ocean, as observed on SSS and Chl*a* maps. The plume generates a strong CO₂ sink that is amplified by strong winds, and reaches up to 12°N (Figure 10). The freshwater plume covers only 10% of the total area, but contributes to almost 20 % of the sink. In winter, this region is either not characterized in previous studies, or considered as dominated by high fCO₂ waters brought by the NBC on the climatology. We observe here that the trapping of CO₂-rich water by NBC rings effect is relatively weak in winter, and the main signal is associated to the filaments they stir.

The north-western tropical Atlantic therefore behaves as a sink of CO₂ in early to mid-February, driven by the cold north Atlantic subtropical waters and the Amazon freshwater plume stirred by NBC rings.



465 **Figure 11: Integrated flux for the [5°-16°N, 59-50°W] domain, and for 3 water masses. For each bar duet, the one on the left in faded colours represents the integrated flux from Landschützer et al., (2020) February climatology, while the one on the right is computed from the reconstructed flux. Same colour code as in Figure 5.**

470 **4 Discussion**

4.1 Integrated air-sea CO₂ flux

The northwestern tropical Atlantic presents a strong seasonal variability of air-sea CO₂ fluxes (Landschützer et al., 2016). In February, waters are the coldest, and we estimate the 5-16N, 59-50W domain to be a strong CO₂ sink of -1.7 TgC month⁻¹ (Figure 11). This region, located at tropical latitudes but combining characteristics of subtropical waters and river outflow, is difficult to represent in large-scale climatologies. Indeed, the sink for the month of February is smaller by a factor 10 in Landschützer et al. (2020), and is also considerably smaller in Takahashi et al., (2009), but the low spatial resolution of this last product doesn't allow for a good quantitative comparison. This region has been rarely observed, and the interannual variability described in Landschützer et al., (2020)'s climatology is therefore rather uncertain. The compensating effect of different years cannot explain entirely the difference of signal observed in February 2020 with respect to the two climatologies.

480

Three water masses mainly contribute to the air-sea CO₂ flux, the NASW, the fresh plume and the NBC retroflection. The NASW contributes to about 60% of the total sink and is not well captured in climatologies, with noticeable differences of more than 20 μatm between the measured $\Delta f\text{CO}_2$ in 2020 and the one computed from Landschützer et al., (2020) and Takahashi et al., (2009) (the closest grid point is considered for this comparison). The retroflection is the main region with a positive air-sea CO₂ flux. Its influence is observed up to 10°N-55°W, but its area is small so its impact on the regional flux is weak. The positive flux of the retroflection is slightly overestimated in the climatologies, but it could also be due to the difficulty to detect the retroflection at the beginning of February. The main difference is that the NBC waters rich in CO₂ are localized in the retroflection area, and are heavily modified when spreading into the Eddy Boulevard.

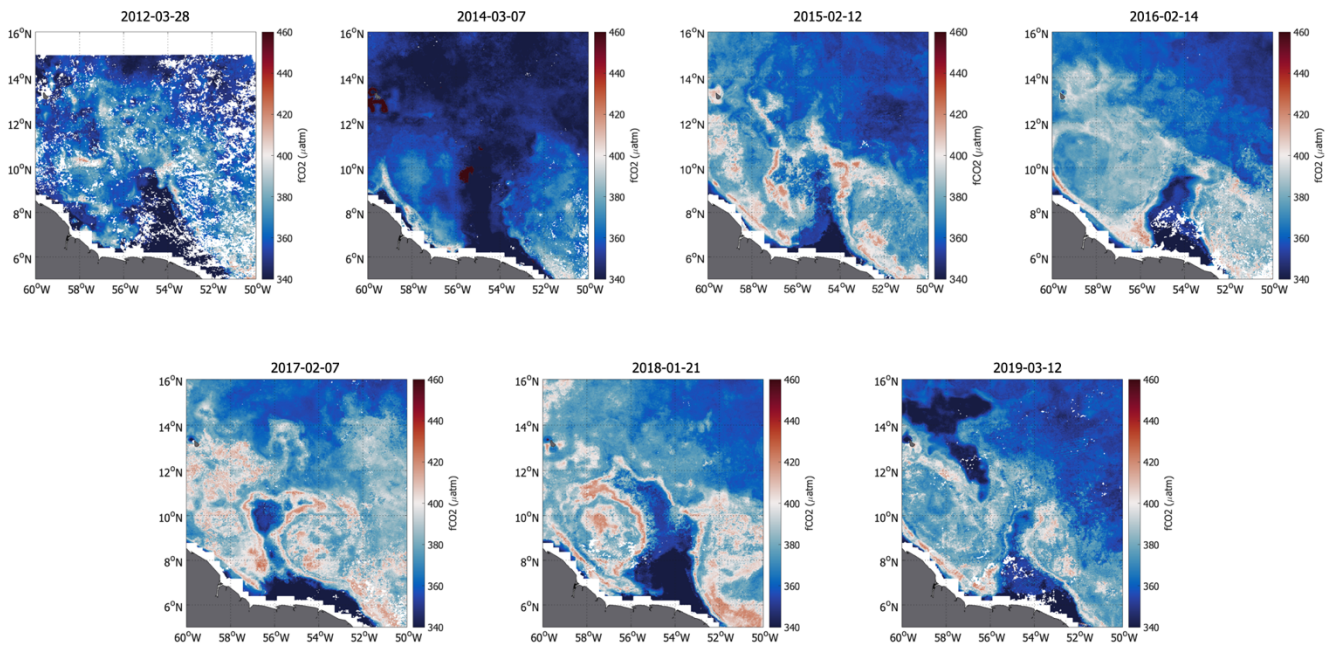
The freshwater plume is a feature previously not well described for this region in winter and we found a contribution of almost 20 % to the sink. The impact of the Amazon River has been overlooked so far in winter, but it accounts for a large part of the salinity and biogeochemical variability. Freshwater from the Amazon is not just located on the shelf, but it can spread northward advected by the strong current variability associated to the NBC rings (Reverdin et al., 2021). These rings are the largest, faster rotating and are the most energetic during boreal winter compared to other seasons (Aroucha et al., 2020). Combined with a seasonal increase in the Amazon's outflow, it induces a large variability in SSS, Chl*a* and fCO₂. The occurrence of freshwater export from the shelf to the open ocean has a strong influence on the salinity and therefore on the mixed layer depth and air-sea heat exchanges (Reverdin et al., 2021). It also strongly impacts the biogeochemistry of the region as the low fCO₂ is due both to the low salinity of the plume waters and to the biological activity. The plume stirred into the open ocean by the NBC rings brings nutrients in a region strongly nutrient-limited, and generates a local winter bloom. This in turns plays an important role on the air-sea CO₂ flux, and is a crucial feature of the southern part of the northwestern tropical Atlantic.

4.2 Extension to other years and interannual variability

Few tropical Atlantic measurements of biogeochemical tracers are available, in particular in the northwestern tropical Atlantic. The EUREC⁴A-OA/ATOMIC campaign provides the first in-situ comprehensive measurements of fCO₂ in this region for the boreal winter season. The reconstruction of fCO₂ maps likely provides a good understanding of the spatial evolution of fCO₂ and air-sea CO₂ fluxes, and is fitted for the months of January-February 2020. Although the processes described here are specific to winter and thus cannot be extended to other seasons, they will be useful to understand the winter variability of other years.

Only a few cruises cross the region according to the SOCAT database between 2010 and 2019 (period with satellite SSS data) and investigating inter-annual variability is not possible. However, we can test the relation developed for 2020 for other years by using selected cruises from the SOCAT database. We thus first use the relationship to reconstruct fCO₂ along the ship tracks (using in-situ SSS and SST and colocalized Chl*a*) and then over the whole region based on satellite products (OSTIA SST, Globcolour Chl*a*, SSS+CCI, detailed in the appendix A). A comparison between the measured and reconstructed fCO₂ for the water masses sampled by the SOCAT cruises (NASW, fresh plume, NBC retroflection, modified NBC) is presented in the

appendix (Table A1). Good agreement is found between the $f\text{CO}_2$ from the SOCAT database and the one reconstructed from the in-situ temperature and salinity, and colocalized Chla for the four water masses (averaged difference of $5.5 \mu\text{atm}$). When comparing reconstructed $f\text{CO}_2$ maps with $f\text{CO}_2$ on ship tracks (Figure A1), the agreement between $f\text{CO}_2$ in various water masses is very clear, even though the spatial structures are sometimes a bit misplaced. This is attributable to the slightly coarser resolution of satellite products not designed specifically for each campaign, to the high spatio-temporal variability of $f\text{CO}_2$ and to missing Chla and SST observations in cloudy areas. February 2020 was mainly cloud free, so that we were able to use high resolution daily SST and Chla . The SSS product used in 2020 is also a daily product. However, for the other years, the satellite Chla (if clouds) and SSS products have a weekly temporal resolution, which smear the fast-moving structures. The gradients between water masses are therefore not always well represented, but we find a good agreement between the $f\text{CO}_2$ of each structure, which is encouraging for future studies on interannual variability in winter.



525

Figure 12: Snapshot of reconstructed $f\text{CO}_2$ for all occurrences of fresh plumes extending at least to 10°N and east of 56°W in January-March 2010-2019 (2010, 2011 and 2013 do not present this type of event).

By identifying the main processes responsible for the variability of the air-sea CO_2 flux in 2020, we can better understand the interannual variability of the region. Indeed, each of the main water mass has its own interannual variability that shapes the CO_2 variability. The northern part of the domain is dominated by the variation of temperature, and therefore its interannual variability is mainly linked to the one of SST. From 32 years monthly mean SST data, the SST standard deviation in the area

530

is relatively weak, and doesn't exceed 0.5°C. The northern sink of CO₂ is therefore rather similar from year to year, coherent with the low standard deviation of the air-sea CO₂ flux computed from Landschützer et al., (2020). Some variability is still
535 observed on the snapshot of the reconstructed fCO₂ (Figure 12), but to a much smaller extent than south of Barbados. For example, the strong sink observed in March 2014 is caused by cold SST anomalies over the whole domain. Some small-scale variability in the northern part of the domain is sometimes correlated to SSS anomalies, as in 2019.

The freshwater plume sampled during EUREC⁴A-OA is a common feature in February. During the 2010-2019 period, events of freshwater reaching the open ocean were observed each year, and freshwater plumes similar to the one described in this
540 paper were observed during 7 out of 10 years from satellite salinity data (Reverdin et al., 2021). Two of the main mechanisms driving the occurrence of the plume are the winds near the Amazon estuary that can induce along shelf transport to the Guyana plateau and the presence of NBC rings. Most of the plume events similar to the one in this study suggest the presence of an anticyclone to its east. This region is commonly crossed by several NBC rings during winter (Jochumsen et al., 2010; Johns et al., 2003; Mélice and Arnault, 2017) but it also is subject to a strong year to year variability that has linkages with the variability
545 of the Amazon River outflow (Aroucha et al., 2020). Therefore, identifying and understanding the processes happening in 2020 should contribute to better assess the interannual variability of fCO₂ as well as air-sea CO₂ fluxes in the northwestern tropical Atlantic during winter. Using a combination of SSS, SST and Chl_a brings information on the biogeochemistry of the area in winter and represent well the mesoscale structure.

5. Conclusion

550 The EUREC⁴A-OA/ATOMIC campaign provides for the first time synoptic measurements related to the air-sea fluxes of CO₂ in the northwestern tropical Atlantic in winter. Six main surface water masses are identified, one of them north of Barbados (North Atlantic Subtropical Water), and the other five (the NBC retroflexion, modified NBC waters, the freshwater plume, the shelf water and the shelf filament) south of Barbados. The investigation highlights the two different regimes of the region. In the northern part, the variability of the CO₂ flux is low and the area is covered by relatively cold, saline and low-chlorophyll
555 NASW. The southern part is highly variable, due to the presence of large mesoscale anticyclonic eddies. In January and February 2020, two NBC rings influence the physical and biogeochemical properties of the region. The NBC retroflexion is characterized by waters with equatorial origins that are relatively warm, saline and high in fCO₂. As the rings separate from the retroflexion, they interact with the surrounding waters, and the initial signal in fCO₂ is dampened. The main impact of the rings is therefore not necessarily on the surface water they transport in their core (eddy trapping), but rather on the filaments
560 they stir off the coast (eddy stirring). A fresh plume from the Amazon River is transported by the coastal current up to the French Guiana shelf in the beginning of February. The NBC rings entrain the plume of freshwater up to 12°N. This plume is fresh, rich in Chl_a and low in fCO₂ and strongly contrasts with the surrounding waters and spreads over ~100 000 km². On the shelf not influenced by the plume, water is relatively saline, high in fCO₂ and Chl_a, probably due to high concentration of

detrital material. As ring A2 propagates westward, it continuously stirs a thin (10 km wide) filament of high $f\text{CO}_2$ shelf water up to 12°N .
565

Based on the ship observations we identify distinct regimes in $f\text{CO}_2$ linked to certain combinations of SST, SSS, and *Chla* properties. We use this information to construct high-resolution maps of $f\text{CO}_2$ and air-sea CO_2 flux using satellite maps of SSS, SST and *Chla*. On average over early to mid-February, the region acts as a strong sink of CO_2 ($-1.7 \text{ TgC}\cdot\text{month}^{-1}$), the sink being ten times smaller in air-sea CO_2 flux climatologies. The NASW is responsible for most of the flux (60%) due to
570 low temperature associated to winter cooling and strong winds. South of Barbados, the region acts also as a sink of CO_2 . The influence of equatorial water is localized to the retroreflection region that acts as a small source of CO_2 . The main feature in this part of the domain is the fresh plume that contributes almost 20% of the total sink.

The processes described here highlight the high variability of air-sea CO_2 fluxes in winter, that are quite different from the ones in summer. These features are relatively common in winter and can be used to better understand the interannual variability of air-sea CO_2 fluxes. The northern part of the domain is driven by the variability in SST, while the southern one is a combination of the interannual variability of temperature, salinity and chlorophyll. It is therefore linked to the year-to-year variability of the NBC rings and the Amazon outflow.
575

This study is limited by the paucity of data in the region and for this time period. More $f\text{CO}_2$ data closer to the coast would help to better quantify the influence of shelf water on the flux. The signature of the NBC rings has been described for only two rings that had different signatures. In order to reach more robust conclusions on the transport of surface NBC water by the rings, more eddies should be observed. The variability of $f\text{CO}_2$ occurs at large and small scale. Salinity is one of the most valuable predictors of $f\text{CO}_2$ south of 10°N , but the satellite salinity resolution is much lower than those of temperature and chlorophyll. To have a more accurate prediction of the $f\text{CO}_2$, a high-resolution SSS product would also be very useful.
580

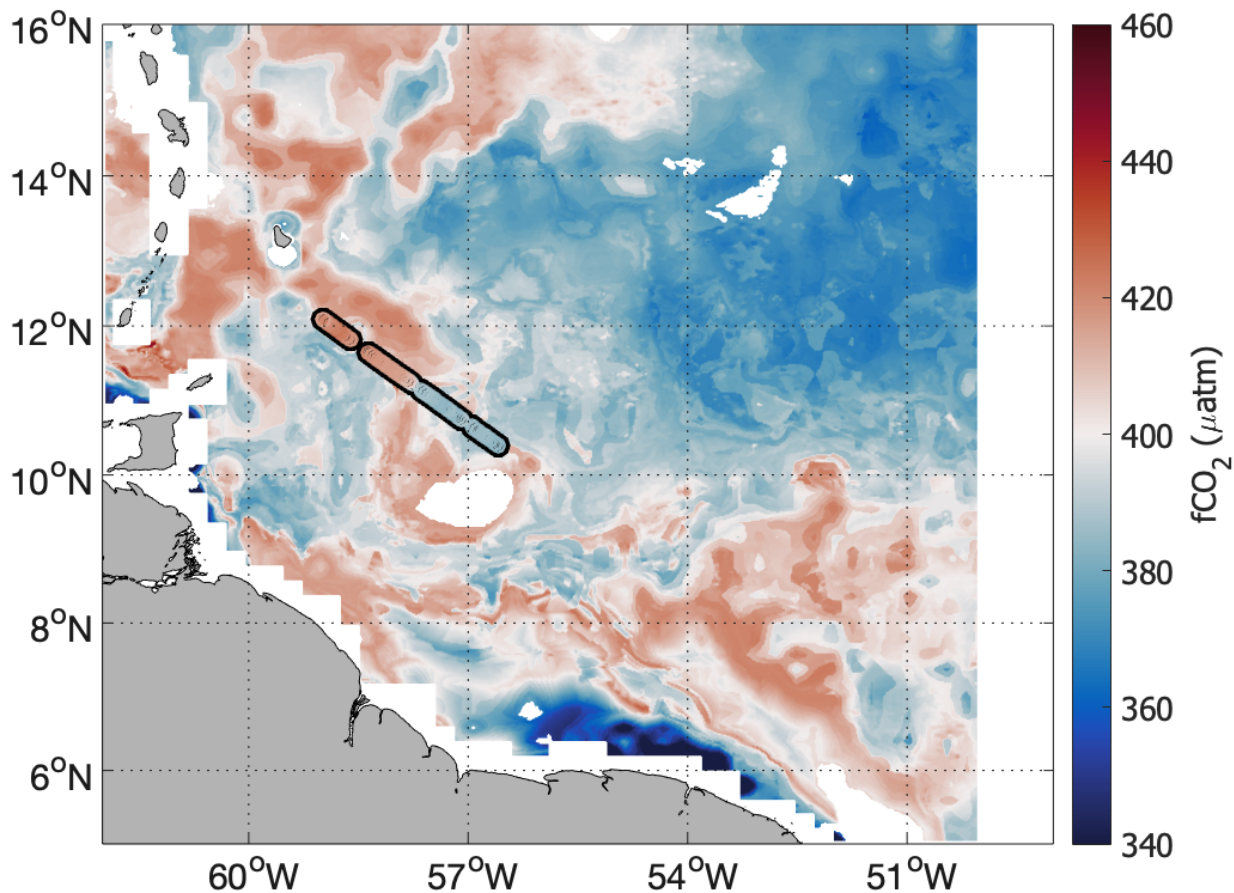
585 **Appendix A**

Due their long time series, the following SST, *Chla* and SSS products are used to reconstruct $f\text{CO}_2$ maps in winter in the northwestern tropical Atlantic for other years than 2020. Results are shown on Figure A1 and Figure 12. They are different than the satellite products used in the main study, that were only available on a short period.

The Operational Sea Surface Temperature and Sea Ice Analysis (OSTIA) SST product, distributed by the CMEMS is used here. Daily maps of SST are produced at a resolution of $1/20^\circ$, available from 1981 to present. OSTIA SST uses most SST data available for a day, from both infrared and microwave inferred SST.
590

Surface *Chla* from GlobColour dataset derived from ocean color at a $1/24^\circ$ resolution is used. It is a merged product from multiple satellite missions' observations (SeaWiFS, MERIS, MODIS, VIIRS NPP, OLCI-A, VIIRS JPSS-1 and OLCI-B). GlobColour data is developed and validated by ACRI-st and distributed by the CMEMS.

595 We also use SMOS and SMAP combined weekly SSS generated by the Climate Change Initiative Sea Surface Salinity (CCI + SSS) project (Boutin et al., 2021, <http://dx.doi.org/10.5285/5920a2c77e3c45339477acd31ce62c3c>). It provides weekly level-3 SSS data from 2010 to 2019 at a spatial resolution of 50 km, a sampled daily on a 25 km x 25 km grid, by combining data from the SMOS, Aquarius, and SMAP missions.



600

Figure A1. fCO₂ reconstructed from OSTIA SST, CCI+SSS and Globcolour Chl*a* for the 23/12/2015 superimposed with the fCO₂ from cruise 642B20151209.

605

	Fresh plume	NBC waters	Modified NBC	NASW
SOCAT fCO₂	316.2	413.4	385.8	349
fCO₂ reconstructed from SOCAT SST & SSS	310.7	410.7	392.9	358.7
Transect date	2016/01/05	2016/01/08	2015/12/23	2013/02/10
Ship Name	Colibri (France)	Colibri (France)	MSC Marianna (Panama)	Benguela Stream (Netherlands)
Expocode	35MJ20151229	35MJ20160107	642B20151209	33RO20130108

Table A1. Comparison for the 4 main water masses between the fCO₂ from SOCAT transect and the fCO₂ reconstructed from in-situ SSS and SST and colocalized Chl_a.

610

Code Availability

Code used in this study can be made available upon reasonable request to the corresponding author.

Data Availability

We benefited from numerous data sets made freely available and listed here: the ADT produced by Ssalto/Duacs distributed
615 by CMEMS (<https://resources.marine.copernicus.eu>), the Chl_a and SST maps produced by CLS (<https://datastore.cls.fr/catalogues/chlorophyll-high-resolution-daily> and <https://datastore.cls.fr/catalogues/sea-surface-temperature-infra-red-high-resolution-daily>), the SMOS L2Q field produced by CATDS (CATDS, 2019) (<https://10.12770/12dba510-cd71-4d4f-9fc1-9cc027d128b0>), the SMAP maps produced by Remote Sensing System (RSS v4 40 km), the CCI+SSS maps produced in the frame of ESA CCI+SSS project
620 (<http://dx.doi.org/10.5285/5920a2c77e3c45339477acd31ce62c3c>), the OSTIA SST and Copernicus -GlobColour Chl_a distributed by the CMEMS (SST_GLO_SST_L4_REP_OBSERVATIONS_010_011 and OCEANCOLOUR_GLO_CHL_L4_REP_OBSERVATIONS_009_082).

The RV Atalante fCO₂ is available on the SEANOE website: doi/10.17882/83578. The RV Ron Brown and RV Merian fCO₂
625 data can be found on the SOCAT database (expocodes 33RO20200106 and 06M220200117 respectively). The Surface Ocean CO₂ Atlas (SOCAT) is an international effort, endorsed by the International Ocean Carbon Coordination Project (IOCCP), the Surface Ocean Lower Atmosphere Study (SOLAS) and the Integrated Marine Biosphere Research program, to deliver a uniformly quality-controlled surface ocean CO₂ database. The many researchers and funding agencies responsible for the collection of data and quality control are thanked for their contributions to SOCAT.

630 **Author contribution**

LO, JB, GR and NL conceptualized the project. LO carried out the measurements and data analysis. LO, JB, GR, NL and PL contributed to result interpretation. PL, MR and RW provided the crucial datasets. LO, MR, SS, JK, ML, TS and CN conducted field work. LO wrote the manuscript with input from all co-authors.

Competing interests

635 Some authors are members of the editorial board of Biogeosciences. The peer-review process was guided by an independent editor, and the authors have also no other competing interests to declare.

Acknowledgements

This research has been supported by the European Research Council (ERC) advanced grant EUREC⁴A (grant agreement no. 694768) under the European Union's Horizon 2020 research and innovation program (H2020), with additional support from
640 CNES (the French National Centre for Space Studies) through the TOSCA SMOS-Ocean, TOEddies, and EUREC⁴A-OA proposals, the French national program LEFE INSU, by IFREMER, the French research fleet, the French research infrastructures AERIS and ODATIS, IPSL, the Chaire Chanel program of the Geosciences Department at ENS and the EUREC⁴A-OA JPI Ocean & Climate program. LO was supported by a scholarship from ENS and Sorbonne Université. We thank Jonathan Fin at the Service National d'Analyse des paramètres Océaniques du CO₂ (SNAPO-CO₂) at LOCEAN for the
645 analysis of DIC and TA samples, and François Baurand at the US IMAGO for the nutrient analysis. Kevin Sullivan performed the data reduction and quality control of data on the Ronald H Brown. We also warmly thank the captain and crew of RVs Atalante, Maria S. Merian and Ronald H. Brown. The measurements on the Ronald H. Brown were supported by the Global Ocean Monitoring and Observation (GOMO) program (fund Ref. 100007298).

References

- 650 Aller, R. C. and Blair, N. E.: Carbon remineralization in the Amazon–Guianas tropical mobile mudbelt: A sedimentary incinerator, *Continental Shelf Research*, 26, 2241–2259, <https://doi.org/10.1016/j.csr.2006.07.016>, 2006.
- Andrié, C., Oudot, C., Genthon, C., and Merlivat, L.: CO₂ fluxes in the tropical Atlantic during FOCAL cruises, 91, 11741–11755, <https://doi.org/10.1029/JC091iC10p11741>, 1986.
- Aroucha, L. C., Veleda, D., Lopes, F. S., Tyaquicã, P., Lefèvre, N., and Araujo, M.: Intra- and Inter-Annual Variability of
655 North Brazil Current Rings Using Angular Momentum Eddy Detection and Tracking Algorithm: Observations From 1993 to 2016, 125, e2019JC015921, <https://doi.org/10.1029/2019JC015921>, 2020.

- Arrigo, K. R.: Marine manipulations, 450, 491–492, <https://doi.org/10.1038/450491a>, 2007.
- Arruda, R., Atamanchuk, D., Cronin, M., Steinhoff, T., and Wallace, D. W. R.: At-sea intercomparison of three underway pCO₂ systems, 18, 63–76, <https://doi.org/10.1002/lom3.10346>, 2020.
- 660 Bakker, D. C. E., Pfeil, B., Landa, C. S., Metzl, N., O'Brien, K. M., Olsen, A., Smith, K., Cosca, C., Harasawa, S., Jones, S. D., Nakaoka, S., Nojiri, Y., Schuster, U., Steinhoff, T., Sweeney, C., Takahashi, T., Tilbrook, B., Wada, C., Wanninkhof, R., Alin, S. R., Balestrini, C. F., Barbero, L., Bates, N. R., Bianchi, A. A., Bonou, F., Boutin, J., Bozec, Y., Burger, E. F., Cai, W.-J., Castle, R. D., Chen, L., Chierici, M., Currie, K., Evans, W., Featherstone, C., Feely, R. A., Fransson, A., Goyet, C., Greenwood, N., Gregor, L., Hankin, S., Hardman-Mountford, N. J., Harlay, J., Hauck, J., Hoppema, M., Humphreys, M. P.,
- 665 Hunt, C. W., Huss, B., Ibánhez, J. S. P., Johannessen, T., Keeling, R., Kitidis, V., Körtzinger, A., Kozyr, A., Krasakopoulou, E., Kuwata, A., Landschützer, P., Lauvset, S. K., Lefèvre, N., Lo Monaco, C., Manke, A., Mathis, J. T., Merlivat, L., Millero, F. J., Monteiro, P. M. S., Munro, D. R., Murata, A., Newberger, T., Omar, A. M., Ono, T., Paterson, K., Pearce, D., Pierrot, D., Robbins, L. L., Saito, S., Salisbury, J., Schlitzer, R., Schneider, B., Schweitzer, R., Sieger, R., Skjelvan, I., Sullivan, K. F., Sutherland, S. C., Sutton, A. J., Tadokoro, K., Telszewski, M., Tuma, M., van Heuven, S. M. A. C., Vandemark, D., Ward, B.,
- 670 Watson, A. J., and Xu, S.: A multi-decade record of high-quality *f*CO₂ data in version 3 of the Surface Ocean CO₂ Atlas (SOCAT), 8, 383–413, <https://doi.org/10.5194/essd-8-383-2016>, 2016.
- Behrenfeld, M. J., O'Malley, R. T., Siegel, D. A., McClain, C. R., Sarmiento, J. L., Feldman, G. C., Milligan, A. J., Falkowski, P. G., Letelier, R. M., and Boss, E. S.: Climate-driven trends in contemporary ocean productivity, 444, 752–755, <https://doi.org/10.1038/nature05317>, 2006.
- 675 Boutin, J., Vergely, J.-L., Reul, N., Catany, R., Koehler, J., Martin, A., Rouffi, F., Arias, M., Chakroun, M., Corato, G., Estella-Perez, V., Guimard, S., Hasson, A., Josey, S., Khvorostyanov, D., Kolodziejczyk, N., Mignot, J., Olivier, L., Reverdin, G., Stammer, D., Supply, A., Thouvenin-Masson, C., Turiel, A., Vialard, J., Cipollini, P., and Donlon, C.: ESA Sea Surface Salinity Climate Change Initiative (Sea_Surface_Salinity_cci): weekly and monthly sea surface salinity products, v03.21, for 2010 to 2020, <https://doi.org/10.5285/5920A2C77E3C45339477ACD31CE62C3C>, 2021.
- 680 Chen, C.-T. A., Huang, T.-H., Fu, Y.-H., Bai, Y., and He, X.: Strong sources of CO₂ in upper estuaries become sinks of CO₂ in large river plumes, *Current Opinion in Environmental Sustainability*, 4, 179–185, <https://doi.org/10.1016/j.cosust.2012.02.003>, 2012.
- Coles, V. J., Brooks, M. T., Hopkins, J., Stukel, M. R., Yager, P. L., and Hood, R. R.: The pathways and properties of the Amazon River Plume in the tropical North Atlantic Ocean, 118, 6894–6913, <https://doi.org/10.1002/2013JC008981>, 2013.
- 685 Dai, A. and Trenberth, K. E.: Estimates of Freshwater Discharge from Continents: Latitudinal and Seasonal Variations, 3, 660–687, [https://doi.org/10.1175/1525-7541\(2002\)003<0660:EOFDFC>2.0.CO;2](https://doi.org/10.1175/1525-7541(2002)003<0660:EOFDFC>2.0.CO;2), 2002.
- Edmond, J. M.: High precision determination of titration alkalinity and total carbon dioxide content of sea water by potentiometric titration, *Deep Sea Research and Oceanographic Abstracts*, 17, 737–750, [https://doi.org/10.1016/0011-7471\(70\)90038-0](https://doi.org/10.1016/0011-7471(70)90038-0), 1970.
- 690 Entekhabi, D., Njoku, E. G., O'Neill, P. E., Kellogg, K. H., Crow, W. T., Edelstein, W. N., Entin, J. K., Goodman, S. D., Jackson, T. J., and Johnson, J.: The soil moisture active passive (SMAP) mission, 98, 704–716, 2010.
- Ffield, A.: North Brazil current rings viewed by TRMM Microwave Imager SST and the influence of the Amazon Plume, *Deep Sea Research Part I: Oceanographic Research Papers*, 52, 137–160, <https://doi.org/10.1016/j.dsr.2004.05.013>, 2005.
- 695 Field, C. B., Behrenfeld, M. J., Randerson, J. T., and Falkowski, P.: Primary Production of the Biosphere: Integrating Terrestrial and Oceanic Components, 281, 237–240, <https://doi.org/10.1126/science.281.5374.237>, 1998.

- Font, J., Camps, A., Borges, A., Martín-Neira, M., Boutin, J., Reul, N., Kerr, Y. H., Hahne, A., and Mecklenburg, S.: SMOS: The challenging sea surface salinity measurement from space, 98, 649–665, 2009.
- Fournier, S., Chapron, B., Salisbury, J., Vandemark, D., and Reul, N.: Comparison of spaceborne measurements of sea surface salinity and colored detrital matter in the Amazon plume, 120, 3177–3192, <https://doi.org/10.1002/2014JC010109>, 2015.
- 700 Fratantoni, D. M. and Glickson, D. A.: North Brazil Current Ring Generation and Evolution Observed with SeaWiFS, *J. Phys. Oceanogr.*, 32, 1058–1074, [https://doi.org/10.1175/1520-0485\(2002\)032<1058:NBCRGA>2.0.CO;2](https://doi.org/10.1175/1520-0485(2002)032<1058:NBCRGA>2.0.CO;2), 2002.
- Fratantoni, D. M. and Richardson, P. L.: The Evolution and Demise of North Brazil Current Rings, 36, 1241–1264, <https://doi.org/10.1175/JPO2907.1>, 2006.
- 705 Friedlingstein, P., O’Sullivan, M., Jones, M. W., Andrew, R. M., Hauck, J., Olsen, A., Peters, G. P., Peters, W., Pongratz, J., Sitch, S., Le Quéré, C., Canadell, J. G., Ciais, P., Jackson, R. B., Alin, S., Aragão, L. E. O. C., Arneeth, A., Arora, V., Bates, N. R., Becker, M., Benoit-Cattin, A., Bittig, H. C., Bopp, L., Bultan, S., Chandra, N., Chevallier, F., Chini, L. P., Evans, W., Florentie, L., Forster, P. M., Gasser, T., Gehlen, M., Gilfillan, D., Gkritzalis, T., Gregor, L., Gruber, N., Harris, I., Hartung, K., Haverd, V., Houghton, R. A., Ilyina, T., Jain, A. K., Joetzjer, E., Kadono, K., Kato, E., Kitidis, V., Korsbakken, J. I., Landschützer, P., Lefèvre, N., Lenton, A., Lienert, S., Liu, Z., Lombardozzi, D., Marland, G., Metzl, N., Munro, D. R., Nabel, 710 J. E. M. S., Nakaoka, S.-I., Niwa, Y., O’Brien, K., Ono, T., Palmer, P. I., Pierrot, D., Poulter, B., Resplandy, L., Robertson, E., Rödenbeck, C., Schwinger, J., Séférian, R., Skjelvan, I., Smith, A. J. P., Sutton, A. J., Tanhua, T., Tans, P. P., Tian, H., Tilbrook, B., van der Werf, G., Vuichard, N., Walker, A. P., Wanninkhof, R., Watson, A. J., Willis, D., Wiltshire, A. J., Yuan, W., Yue, X., and Zaehle, S.: Global Carbon Budget 2020, 12, 3269–3340, <https://doi.org/10.5194/essd-12-3269-2020>, 2020.
- 715 Garraffo, Z. D., Johns, W. E., P.Chassignet, E., and Goni, G. J.: North Brazil Current rings and transport of southern waters in a high resolution numerical simulation of the North Atlantic, in: Elsevier Oceanography Series, vol. 68, edited by: Goni, G. J. and Malanotte-Rizzoli, P., Elsevier, 375–409, [https://doi.org/10.1016/S0422-9894\(03\)80155-1](https://doi.org/10.1016/S0422-9894(03)80155-1), 2003.
- Goni, G. J. and Johns, W. E.: A census of North Brazil Current Rings observed from TOPEX/POSEIDON altimetry: 1992–1998, 28, 1–4, <https://doi.org/10.1029/2000GL011717>, 2001.
- 720 Grodsky, S. A., Vandemark, D., and Feng, H.: Assessing Coastal SMAP Surface Salinity Accuracy and Its Application to Monitoring Gulf of Maine Circulation Dynamics, 10, 1232, <https://doi.org/10.3390/rs10081232>, 2018.
- Ibáñez, J. S. P., Araujo, M., and Lefèvre, N.: The overlooked tropical oceanic CO₂ sink, 43, 3804–3812, <https://doi.org/10.1002/2016GL068020>, 2016.
- Jochumsen, K., Rhein, M., Hüttl-Kabus, S., and Böning, C. W.: On the propagation and decay of North Brazil Current rings, 115, <https://doi.org/10.1029/2009JC006042>, 2010.
- 725 Johns, W. E., Lee, T. N., Schott, F. A., Zantopp, R. J., and Evans, R. H.: The North Brazil Current retroflexion: Seasonal structure and eddy variability, 95, 22103–22120, <https://doi.org/10.1029/JC095iC12p22103>, 1990.
- Johns, W. E., Zantopp, R. J., and Goni, Gustavo. J.: Cross-gyre transport by North Brazil Current rings, in: Elsevier Oceanography Series, vol. 68, edited by: Goni, G. J. and Malanotte-Rizzoli, P., Elsevier, 411–441, [https://doi.org/10.1016/S0422-9894\(03\)80156-3](https://doi.org/10.1016/S0422-9894(03)80156-3), 2003.
- 730 Karstensen, J., Lavik, G., Acquistapace, C., Bagheri, G., Begler, C., Bendinger, A., Bodenschatz, E., Böck, T., Güttler, J., Hall, K., Körner, M., Kopp, A., Lange, D., Mehlmann, M., Nordsiek, F., Reus, K., Ribbe, J., Philippi, M., Piosek, S., Ritschel, M., Tschitschko, B., and Wiskandt, J.: EUREC4A Campaign, Cruise No. MSM89, 17. January - 20. February 2020, Bridgetown

- (Barbados) - Bridgetown (Barbados), The ocean mesoscale component in the EUREC4A field study, Gutachterpanel Forschungsschiffe, Bonn, 70 pp., https://doi.org/10.2312/cr_msm89, 2020.
- 735 Kerr, Y. H., Waldteufel, P., Wigneron, J.-P., Delwart, S., Cabot, F., Boutin, J., Escorihuela, M.-J., Font, J., Reul, N., and Gruhier, C.: The SMOS mission: New tool for monitoring key elements of the global water cycle, 98, 666–687, 2010.
- Körtzinger, A.: A significant CO₂ sink in the tropical Atlantic Ocean associated with the Amazon River plume, 30, <https://doi.org/10.1029/2003GL018841>, 2003.
- 740 Landschützer, P., Gruber, N., Bakker, D. C. E., and Schuster, U.: Recent variability of the global ocean carbon sink, 28, 927–949, <https://doi.org/10.1002/2014GB004853>, 2014.
- Landschützer, P., Gruber, N., and Bakker, D. C. E.: Decadal variations and trends of the global ocean carbon sink, 30, 1396–1417, <https://doi.org/10.1002/2015GB005359>, 2016.
- Landschützer, P., Laruelle, G. G., Roobaert, A., and Regnier, P.: A uniform pCO₂ climatology combining open and coastal oceans, 12, 2537–2553, <https://doi.org/10.5194/essd-12-2537-2020>, 2020.
- 745 Laxenaire, R., Speich, S., Blanke, B., Chaigneau, A., Pegliasco, C., and Stegner, A.: Anticyclonic Eddies Connecting the Western Boundaries of Indian and Atlantic Oceans, 123, 7651–7677, <https://doi.org/10.1029/2018JC014270>, 2018.
- Lefèvre, N., Diverrés, D., and Gallois, F.: Origin of CO₂ undersaturation in the western tropical Atlantic, 62, 595–607, <https://doi.org/10.1111/j.1600-0889.2010.00475.x>, 2010.
- 750 Masson-Delmotte, V., Zhai, P., Pirani, A., Connors, S. L., Péan, C., Berger, S., Caud, N., Chen, Y., Goldfarb, L., Gomis, M. I., Huang, M., Leitzell, K., Lonnoy, E., Matthews, J. B. R., Maycock, T. K., Waterfield, T., Yelekçi, Ö., Yu, R., and Zhou, B. (Eds.): *Climate Change 2021: The Physical Science Basis. Contribution of Working Group I to the Sixth Assessment Report of the Intergovernmental Panel on Climate Change*, Cambridge University Press, 2021.
- 755 Medeiros, P. M., Seidel, M., Ward, N. D., Carpenter, E. J., Gomes, H. R., Niggemann, J., Krusche, A. V., Richey, J. E., Yager, P. L., and Dittmar, T.: Fate of the Amazon River dissolved organic matter in the tropical Atlantic Ocean, 29, 677–690, <https://doi.org/10.1002/2015GB005115>, 2015.
- Mélice, J.-L. and Arnault, S.: Investigation of the Intra-Annual Variability of the North Equatorial Countercurrent/North Brazil Current Eddies and of the Instability Waves of the North Tropical Atlantic Ocean Using Satellite Altimetry and Empirical Mode Decomposition, 34, 2295–2310, <https://doi.org/10.1175/JTECH-D-17-0032.1>, 2017.
- 760 Mu, L., Gomes, H. do R., Burns, S. M., Goes, J. I., Coles, V. J., Rezende, C. E., Thompson, F. L., Moura, R. L., Page, B., and Yager, P. L.: Temporal Variability of Air-Sea CO₂ flux in the Western Tropical North Atlantic Influenced by the Amazon River Plume, 35, e2020GB006798, <https://doi.org/10.1029/2020GB006798>, 2021.
- Muller-Karger, F. E., McClain, C. R., and Richardson, P. L.: The dispersal of the Amazon's water, 333, 56–59, <https://doi.org/10.1038/333056a0>, 1988.
- 765 Olivier, L., Labaste, M., Noisel, C., and Lefevre, N.: Underway fCO₂ distribution during the EUREC4A-OA experiment, <https://doi.org/10.17882/83578>, 2020.
- Piepmeyer, J. R., Focardi, P., Horgan, K. A., Knuble, J., Ehsan, N., Lucey, J., Brambora, C., Brown, P. R., Hoffman, P. J., and French, R. T.: SMAP L-band microwave radiometer: Instrument design and first year on orbit, 55, 1954–1966, 2017.

- 770 Pierrot, D., Neill, C., Sullivan, K., Castle, R., Wanninkhof, R., Lüger, H., Johannessen, T., Olsen, A., Feely, R. A., and Cosca, C. E.: Recommendations for autonomous underway pCO₂ measuring systems and data-reduction routines, *Deep Sea Research Part II: Topical Studies in Oceanography*, 56, 512–522, <https://doi.org/10.1016/j.dsr2.2008.12.005>, 2009.
- Poisson, A., Metzl, N., Brunet, C., Schauer, B., Bres, B., Ruiz-Pino, D., and Louanchi, F.: Variability of sources and sinks of CO₂ in the western Indian and southern oceans during the year 1991, 98, 22759–22778, <https://doi.org/10.1029/93JC02501>, 1993.
- 775 Pörtner, H.-O., Roberts, D. C., Masson-Delmotte, V., Zhai, P., Tignor, M., Poloczanska, E., and Weyer, N. M.: The ocean and cryosphere in a changing climate, 2019.
- 780 Quinn, P. K., Thompson, E. J., Coffman, D. J., Baidar, S., Bariteau, L., Bates, T. S., Bigorre, S., Brewer, A., de Boer, G., de Szoeko, S. P., Drushka, K., Foltz, G. R., Intrieri, J., Iyer, S., Fairall, C. W., Gaston, C. J., Jansen, F., Johnson, J. E., Krüger, O. O., Marchbanks, R. D., Moran, K. P., Noone, D., Pezoa, S., Pincus, R., Plueddemann, A. J., Pöhlker, M. L., Pöschl, U., Quinones Melendez, E., Royer, H. M., Szczodrak, M., Thomson, J., Upchurch, L. M., Zhang, C., Zhang, D., and Zuidema, P.: Measurements from the RV *Ronald H. Brown* and related platforms as part of the Atlantic Tradewind Ocean-Atmosphere Mesoscale Interaction Campaign (ATOMIC), 13, 1759–1790, <https://doi.org/10.5194/essd-13-1759-2021>, 2021.
- Reverdin, G., Olivier, L., Foltz, G. R., Speich, S., Karstensen, J., Horstmann, J., Zhang, D., Laxenaire, R., Carton, X., Branger, H., Carrasco, R., and Boutin, J.: Formation and Evolution of a Freshwater Plume in the Northwestern Tropical Atlantic in February 2020, 126, e2020JC016981, <https://doi.org/10.1029/2020JC016981>, 2021.
- 785 Richardson, P. L., Hufford, G. E., Limeburner, R., and Brown, W. S.: North Brazil Current retroflection eddies, 99, 5081–5093, <https://doi.org/10.1029/93JC03486>, 1994.
- Schott, F. A., Fischer, J., and Stramma, L.: Transports and Pathways of the Upper-Layer Circulation in the Western Tropical Atlantic, 28, 1904–1928, [https://doi.org/10.1175/1520-0485\(1998\)028<1904:TAPOTU>2.0.CO;2](https://doi.org/10.1175/1520-0485(1998)028<1904:TAPOTU>2.0.CO;2), 1998.
- 790 Speich, S. and The Embarked Science Team: EUREC4A-OA. Cruise Report. 19 January – 19 February 2020. Vessel : L'ATALANTE, 2021.
- 795 Stevens, B., Bony, S., Farrell, D., Ament, F., Blyth, A., Fairall, C., Karstensen, J., Quinn, P. K., Speich, S., Acquistapace, C., Aemisegger, F., Albright, A. L., Bellenger, H., Bodenschatz, E., Caesar, K.-A., Chewitt-Lucas, R., de Boer, G., Delanoë, J., Denby, L., Ewald, F., Fildier, B., Forde, M., George, G., Gross, S., Hagen, M., Hausold, A., Heywood, K. J., Hirsch, L., Jacob, M., Jansen, F., Kinne, S., Klocke, D., Kölling, T., Konow, H., Lothon, M., Mohr, W., Naumann, A. K., Nuijens, L., Olivier, L., Pincus, R., Pöhlker, M., Reverdin, G., Roberts, G., Schnitt, S., Schulz, H., Siebesma, A. P., Stephan, C. C., Sullivan, P., Touzé-Peiffer, L., Vial, J., Vogel, R., Zuidema, P., Alexander, N., Alves, L., Arix, S., Asmath, H., Bagheri, G., Baier, K., Bailey, A., Baranowski, D., Baron, A., Barrau, S., Barrett, P. A., Batier, F., Behrendt, A., Bendinger, A., Beucher, F., Bigorre, S., Blades, E., Blossy, P., Bock, O., Böing, S., Bossert, P., Bourras, D., Bouruet-Aubertot, P., Bower, K., Branellec, P., Branger, H., Brennek, M., Brewer, A., Brilouet, P.-E., Brüggemann, B., Buehler, S. A., Burke, E., Burton, R., Calmer, R., Canonici, J.-C., Carton, X., Cato Jr., G., Charles, J. A., Chazette, P., Chen, Y., Chilinski, M. T., Choularton, T., Chuang, P., Clarke, S., Coe, H., Cornet, C., Coutris, P., et al.: EUREC⁴A, 13, 4067–4119, <https://doi.org/10.5194/essd-13-4067-2021>, 2021.
- 800 Stum, J., Tebri, H., Lehodey, P., Senina, I., Greiner, E., and Lucas, M.: NRT operational chlorophyll maps calculation for marine applications, 1, n.d.
- 805 Subramaniam, A., Yager, P. L., Carpenter, E. J., Mahaffey, C., Björkman, K., Cooley, S., Kustka, A. B., Montoya, J. P., Sañudo-Wilhelmy, S. A., Shipe, R., and Capone, D. G.: Amazon River enhances diazotrophy and carbon sequestration in the tropical North Atlantic Ocean, *PNAS*, 105, 10460–10465, <https://doi.org/10.1073/pnas.0710279105>, 2008.

Takahashi, T., Olafsson, J., Goddard, J. G., Chipman, D. W., and Sutherland, S. C.: Seasonal variation of CO₂ and nutrients in the high-latitude surface oceans: A comparative study, 7, 843–878, <https://doi.org/10.1029/93GB02263>, 1993.

810 Takahashi, T., Sutherland, S. C., Sweeney, C., Poisson, A., Metzl, N., Tilbrook, B., Bates, N., Wanninkhof, R., Feely, R. A., Sabine, C., Olafsson, J., and Nojiri, Y.: Global sea–air CO₂ flux based on climatological surface ocean pCO₂, and seasonal biological and temperature effects, *Deep Sea Research Part II: Topical Studies in Oceanography*, 49, 1601–1622, [https://doi.org/10.1016/S0967-0645\(02\)00003-6](https://doi.org/10.1016/S0967-0645(02)00003-6), 2002.

815 Takahashi, T., Sutherland, S. C., Wanninkhof, R., Sweeney, C., Feely, R. A., Chipman, D. W., Hales, B., Friederich, G., Chavez, F., Sabine, C., Watson, A., Bakker, D. C. E., Schuster, U., Metzl, N., Yoshikawa-Inoue, H., Ishii, M., Midorikawa, T., Nojiri, Y., Körtzinger, A., Steinhoff, T., Hoppema, M., Olafsson, J., Arnarson, T. S., Tilbrook, B., Johannessen, T., Olsen, A., Bellerby, R., Wong, C. S., Delille, B., Bates, N. R., and de Baar, H. J. W.: Climatological mean and decadal change in surface ocean pCO₂, and net sea–air CO₂ flux over the global oceans, *Deep Sea Research Part II: Topical Studies in Oceanography*, 56, 554–577, <https://doi.org/10.1016/j.dsr2.2008.12.009>, 2009.

820 Tennekes, H.: The Logarithmic Wind Profile, 30, 234–238, [https://doi.org/10.1175/1520-0469\(1973\)030<0234:TLWP>2.0.CO;2](https://doi.org/10.1175/1520-0469(1973)030<0234:TLWP>2.0.CO;2), 1973.

Wanninkhof, R.: Relationship between wind speed and gas exchange over the ocean revisited, 12, 351–362, <https://doi.org/10.4319/lom.2014.12.351>, 2014.

825 Wanninkhof, R., Lewis, E., Feely, R. A., and Millero, F. J.: The optimal carbonate dissociation constants for determining surface water pCO₂ from alkalinity and total inorganic carbon, *Marine Chemistry*, 65, 291–301, [https://doi.org/10.1016/S0304-4203\(99\)00021-3](https://doi.org/10.1016/S0304-4203(99)00021-3), 1999.

Weiss, R. F.: Carbon dioxide in water and seawater: the solubility of a non-ideal gas, *Marine Chemistry*, 2, 203–215, [https://doi.org/10.1016/0304-4203\(74\)90015-2](https://doi.org/10.1016/0304-4203(74)90015-2), 1974.

830 Wilson, W. D., Johns, W. E., and Garzoli, S. L.: Velocity structure of North Brazil Current rings, 29, 114-1-114-4, <https://doi.org/10.1029/2001GL013869>, 2002.

835